On the Southern Hemisphere stratospheric response to ENSO and its impacts on tropospheric circulation

Kane A. Stone[a], Susan Solomon[a], David W. J. Thompson[b], Douglas E. Kinnison[c], John C. Fyfe[d]

[a] Department of Earth, Atmospheric, and Planetary Sciences, Massachusetts Institute of Technology, Cambridge, MA, USA

[b] Department of Atmospheric Science, Colorado State University, Fort Collins, CO, USA

[c] Atmospheric Chemistry Observations and Modeling Laboratory, National Center for Atmospheric Research, Boulder, CO, USA

[d] Canadian Centre for Climate Modelling and Analysis, Environment and Climate Change Canada, Victoria, British Columbia, V8W 2Y2, Canada

Corresponding author: Kane A. Stone, stonek@mit.edu

ABSTRACT

As the leading mode of Pacific variability, the El Niño-Southern Oscillation (ENSO) causes vast and wide-spread climatic impacts, including in the stratosphere. Following discovery of a stratospheric pathway of ENSO to the Northern Hemisphere surface, here we aim to investigate if there is a substantial Southern Hemisphere (SH) stratospheric pathway in relation to austral winter ENSO events. Large stratospheric anomalies connected to ENSO occur on average at high SH latitudes as early as August, peaking at around 10 hPa. An overall colder austral spring Antarctic stratosphere is generally associated with the warm phase of the ENSO cycle, and vice versa. This behavior is robust among reanalysis and six separate model ensembles encompassing two different model frameworks. A stratospheric pathway is identified by separating ENSO events that exhibit a stratospheric anomaly from those that don't and comparing to stratospheric extremes that occur during neutral-ENSO years. The tropospheric eddy-driven jet response to the stratospheric ENSO pathway is the most robust in the spring following a La Niña, but extends into summer, and is more zonally-symmetric compared to the tropospheric ENSO teleconnection. The magnitude of the stratospheric pathway is weaker compared to the tropospheric pathway and therefore when it is present, has a secondary role. For context, the magnitude is approximately half that of the eddy-driven jet modulation due to austral spring ozone depletion in the model simulations. This work establishes that the stratospheric circulation acts as an intermediary in coupling ENSO variability to variations in the austral spring and summer tropospheric circulation.

1. Introduction

Southern Hemisphere (SH) tropospheric climate variability is connected to the El Niño Southern Oscillation (ENSO), particularly during the austral summer period. Additionally, strong ENSO events are also known to impact the stratospheric circulation, predominantly in the Northern Hemisphere (NH) winter, and subsequently providing a "stratospheric pathway" onto NH surface climate (Butler et al. 2014; Domeisen et al. 2019). This leads to the questions: To what extent does austral winter ENSO also modulate the SH austral spring stratosphere? And if so, does the SH stratosphere provide a pathway through which ENSO variability influences the SH tropospheric circulation?

Sea surface temperature (SST) variability in the tropical Pacific region is dominated by ENSO (Bjerknes 1969; Wyrtki 1975; Rasmusson and Carpenter 1982). The classic ENSO description is the leading mode of variability in tropical Pacific SSTs. The ENSO events typically begin in June–August, peak in December–March, and diminish by April–May (Trenberth 1997). They have far-reaching global weather impacts, commonly referred to as teleconnections (Bjerknes 1969; Liu and Alexander 2007; Horel and Wallace 1981). For example, El Niño and La Niña events are associated with a disruption in the Walker circulation, a tropical Pacific zonal circulation pattern (Lindzen and Nigam 1987), causing changes in rainfall in both Australia (e.g. McBride and Nicholls 1983; King et al. 2015) and the Americas (e.g. Grimm & Tedeschi, 2009; Ropelewski & Halpert, 1986).

In the SH, ENSO is linked to the South Pacific Convergence Zone (SPCZ), a band of convection in the South Pacific (Trenberth 1984), and the Pacific-South American (PSA) pattern, a quasi-stationary Rossby wave train emanating from the equatorial Pacific towards the South East Pacific and then equatorward in the Atlantic (Karoly 1988; Mo and Ghil 1987; Mo and Paegle 2001). Interannual variability of the tropospheric circulation in the SH is

63 linked to the PSA (Garreaud & Battisti, 1999). Further, SH regional variability within 180-
64 360°E is dominated by two quasi-stationary anti-cyclones with strengths that are negatively
65 correlated to the PSA (Hobbs and Raphael 2010). The occurrence of blocking over the South
66 Pacific, along the PSA track, is modulated strongly by ENSO (Renwick 1998; Renwick and
67 Revell 1999). Recent studies have also suggested that the PSA may represent part of the
68 zonal asymmetric structure of the Southern Annular Mode (SAM) (Irving and Simmonds
69 2016). Therefore, the connection of ENSO to SH circulation is notable, especially in the
70 South Pacific region.

71 While ENSO is the leading mode of variability in the tropics, the SAM is a leading mode
72 of variability within the SH extratropics, and is described as a change in sea level pressure
73 between the SH mid-latitudes and polar regions (Kidson 1988; Karoly, 1990; Kidson &
74 Sinclair, 1995; Hartmann & Lo, 1998; Thompson and Wallace 2000). A positive SAM is
75 associated with lower sea level pressure over Antarctica, and higher pressure in the mid-
76 latitudes, and is strongly coupled to the location of the eddy-driven jet stream and therefore
77 Rossby-wave induced weather fronts (Thompson & Wallace, 2000; Lorenz and Hartmann
78 2001), where a positive SAM denotes a poleward shift of the jet. The connection between
79 ENSO and SAM has widely been documented as negatively correlated, with ENSO
80 projecting strongly onto the SAM (Seager et al. 2003; L'Heureux and Thompson 2006; Fogt
81 et al. 2011; Lim et al. 2013; Wang et al. 2013). However, this relationship may be dependent
82 on the strength of ENSO (Kim et al., 2017). Additionally, Fogt et al. (2012) showed that
83 zonal asymmetries in the SAM during austral spring and summer are closely tied to ENSO,
84 especially in the South Pacific, and can have regional temperature impacts.

85 A number of studies using different models and approaches have examined the influence
86 of springtime Antarctic ozone depletion that has occurred in the last few decades on the

87 austral summer SAM (Thompson and Solomon 2002; Arblaster and Meehl 2006; Son et al.
88 2009; Polvani et al. 2011; Thompson et al. 2011). Stratosphere-troposphere coupling in the
89 SH is also known to occur as early as austral spring after wintertime anomalies in the upper
90 stratosphere occur due to planetary wave breaking (Thompson et al. 2005; Lim et al. 2018).
91 This raises the question of linkages between wintertime ENSO and stratospheric ozone
92 impacts on the SAM.

93 Past studies of ENSO teleconnections into the stratosphere have shown large disturbances
94 in the polar stratosphere temperatures, particularly in the NH and during austral summer
95 (Domeisen et al., 2019 and references therein), the time period when ENSO peaks (Trenberth
96 1997), and heat transport is largest into the NH stratosphere (e. g. McIntyre & Palmer, 1983).
97 In the SH, Central Pacific (where the large SST anomalies are located further west) El Niño
98 events have been shown to have a large impact on the SH stratosphere due to a more
99 enhanced Rossby wave train along the SPCZ (Hurwitz et al. 2011; Yang et al. 2015;
100 Domeisen et al. 2019). Hurwitz et al. (2011) showed that September–November Eastern
101 Pacific El Niño had little impact on the SH stratosphere, while Simpson et al. (2011) reported
102 a strong response in the SH mid-latitudes during austral summer. A recent study suggested
103 that correlations between ENSO and the SH stratosphere are largest a year after an ENSO
104 event, and typically display a dipole structure between the upper and lower stratosphere (Lin
105 and Qian 2019). Whereas, other studies have showed a lag correlation between the SH spring
106 stratosphere and the previous June Central Tropical Pacific SST variability (Evtushevsky et
107 al. 2015; Lim et al. 2018). Evtushevsky et al. (2019) also showed using reanalysis that the SH
108 stratosphere connection to the central tropical Pacific has strengthened in recent decades in
109 the austral spring. In this study, using reanalysis and multiple model ensembles with different
110 greenhouse gas (GHG) and ozone depleting substance (ODS) scenarios, we focus on austral

111 winter ENSO, which allows the characterization of spring and summer anomalies in the
112 stratosphere (an important time period for stratosphere-troposphere coupling). Using multiple
113 ensembles, we analyze ENSO's tropospheric teleconnections onto the SH eddy-driven jet
114 under different GHG and ODS scenarios.

115 Here we aim to separate both a tropospheric and stratospheric pathway of ENSO onto SH
116 austral spring and summer circulation, with a focus on spring. This complements the work
117 done by Butler et al. (2014) for the NH, where both a tropospheric and stratospheric pathway
118 of ENSO to the troposphere was identified during boreal autumn and winter. In that study,
119 ENSO events of either polarity were found to be more likely to coincide with a sudden
120 stratospheric warming (SSW). The stratospheric pathway was shown to affect climate over
121 the North Atlantic and Eurasian region. Separation of the stratospheric and tropospheric
122 pathways of ENSO is also discussed at length in (Jiménez-Esteve and Domeisen 2018, 2020).
123 However, as the SH stratosphere only rarely experiences SSWs, here we aim to investigate
124 how ENSO variability affects both warm and cold SH polar stratospheres, and identify any
125 differing effects from stratospheric and tropospheric pathways to SH tropospheric circulation.

126 2. Reanalysis and Climate Model Ensembles

127 In this study we use reanalysis data as well as six different model ensembles
128 encompassing two model frameworks, described below and in Table 1.

129 The model datasets are compared to a reanalysis assimilated by observations, specifically
130 the JRA-55 global reanalysis (Kobayashi et al. 2015). This reanalysis's feature is its temporal
131 coverage, extending from 1958–present, with years 1958–2019 used in this study. Monthly
132 mean JRA-55 data is used at 1.25° latitude by 1.25° horizontal resolution on 37 pressure
133 levels up to 1 hPa. It is important to note here that the earlier years 1958–1979 (before the

satellite era) in JRA-55 have substantially less assimilated observations, and therefore requires more caution in its use. When, comparing the analysis presented here to identical analysis over the satellite era of 1979–2019, very similar results are obtained. Therefore, we opted to use the full JRA-55 time series to reduce sampling uncertainty.

Four model ensembles with differing ozone depleting substance (ODS) and greenhouse gas (GHG) concentrations (see Table 1) (Stone et al. 2018), were run using the high-top coupled chemistry-climate model Whole Atmosphere Community Climate Model (WACCM4), which is based on the Community Earth System Model, version 1 (CESM1), and is a fully coupled climate model that incorporates atmosphere, ocean, land, and sea ice modules (*Marsh et al.*, 2013; *Garcia et al.*, 2017). The setup of the model used here has a horizontal resolution of 1.9° latitude by 2.5° longitude and 66 vertical levels up to 5.1×10^{-6} hPa (~140 km). The chemical scheme used is the Model of OZone And Related Tracers (MOZART) (*Kinnison et al.*, 2007) and has been shown to accurately simulate polar ozone depletion and levels of chlorine reservoir species (*Solomon et al.*, 2015, 2016). The ocean model is the Parallel Ocean Program (POP), version 2, and is fully coupled (therefore the ENSO events for each ensemble member are different). The setup used has a repeated cyclic 28 month quasi-biennial oscillation (QBO), no solar cycle or solar proton events, and updated sulfate area densities including 21st century volcanic eruptions (*Mills et al.*, 2016; *Neely and Schmidt*, 2016). The four different WACCM ensembles employ different GHG and ODS forcings, with the naming scheme describing the relative forcings. They are all spun up from Chemistry Climate Model Initialization simulations beginning in 1955. Two simulations have evolving GHG and ODS concentrations, but over different time periods, i.e. WACCM-GHG_HODS_H over 1995–2024, and WACCM-GHG_LODS_L over 1955–1979. The subscript L's and H's denote low or high GHG and ODS forcings, respectively, and are designed to be able

158 to obtain the important differences of the WACCM ensembles directly from the title. The
159 other two simulations are WACCM-GHG$_L$ODS$_H$, and WACCM-GHG$_H$ODS$_L$, both run over
160 1995–2024. WACCM-GHG$_L$ODS$_H$ has fixed GHGs at 1960 levels and evolving ODSs, while
161 WACCM-GHG$_H$ODS$_L$ has fixed ODSs at 1960 levels and evolving GHGs. In WACCM-
162 GHG$_H$ODS$_L$, the ODS$_L$ term differs from that in the WACCM-GHG$_L$ODS$_L$ as it has evolving
163 ODSs over 1955–1979 compared to fixed ODSs at 1960 levels. The naming convention is the
164 same as it is designed to convey relative ODS levels (See Table 1 for more information). The
165 four ensembles each consist of 10 members, and are further classified in Table 1.
166 Initialization of the model ensemble members commences from slightly differing initial air
167 temperatures, as is standard in such simulations (*Kay et al.*, 2015; *Solomon et al.*, 2017).

168 We also employ the CESM-large ensemble (LENS), described in detail in Kay et al.
169 (2015). The main difference of this ensemble as compared to WACCM is that it employs a
170 lower model top of ~4 hPa with prescribed rather than coupled ozone fields (see Table 1 for
171 details). In this study, we use all 40 members of LENS over the time period of 1995–2024,
172 similar to the WACCM simulations described above. LENS also employs a prescribed QBO
173 nudged to observed fields.

174 We also examine results from the CanESM2 model's "historical" dataset, which consists
175 of 50 members. The model and its ensembles are described in detail in Arora et al. (2011) and
176 Fyfe et al. (2017). This model is a spectral model with independent architectural structure to
177 that of CESM. Similarly to LENS, CanESM2 has a relatively low top of 1 hPa and prescribed
178 ozone fields (see Table 1). CanESM2 does not simulate or prescribe a QBO.

179 ## 3. Methods

The ENSO index was calculated using principal component analysis of sea surface temperatures over the latitude-longitude range of -30–30°N and 140–260°E. The first empirical orthogonal function (EOF) gives a representation of the Eastern Pacific-ENSO (hereafter referred to as ENSO). A June–August seasonal index is calculated by first forming monthly anomalies over the respective time periods. June–August seasonal averages are then calculated and linearly detrended. We next compute the EOFs over the ENSO latitude-longitude area described above by calculating the eigenvalues of the covariance matrix. The time period of June–August was chosen for two reasons: (1) A lag correlation analysis of monthly ENSO indices for the SH cold season from April–September shows that the anomalies are largest in the Antarctic polar stratosphere from a June ENSO in all model simulations, and August ENSO in JRA55 (although the anomalies are still large in JRA55 from June ENSO events). (2) ENSO events typically begin in austral winter and peak in austral summer before diminishing. Therefore, any austral winter ENSO events that disturb the SH stratosphere will also likely continue to strengthen into the summer. This means the SH troposphere will likely experience austral summer teleconnections from the same ENSO event that disturbed the stratosphere. Therefore, a June–August seasonal ENSO index was chosen.

Composite analysis of ENSO events were performed following Deser et al. (2017), by normalizing the seasonal ENSO index by its seasonal standard deviation. Then, any values above/below 1/-1 standard deviations are described as El Niño/La Niña events. ENSO composite differences were calculated by first detrending the respective fields, with a linear breakpoint imposed in the year 2000 for both stratospheric and tropospheric fields to account for ozone recovery (this was not done for the WACCM-GHG_HODS_L that did not have ozone depletion), then subtracting El Niño years from La Niña years. Significance of the ENSO

composite differences is obtained using a two-tailed two sample t-test at the 95th or 90th percentile with sample sizes equal to the number of El Niño and La Niña events respectively.

Using this composite difference method described above, the surface temperature differences associated with a June–August ENSO in our analysis are shown in Figure 1 for JRA-55, WACCM-GHG$_H$ODS$_H$, CanESM2, and LENS. There is good representation of the ENSO structure in all ensembles compared to JRA-55. The most noticeable differences are that the WACCM-GHG$_H$ODS$_H$ ensemble has a larger SST difference in the eastern Pacific compared to the reanalysis and the other models, and the location of largest SST difference in JRA-55 is concentrated farther eastward than the models, especially compared to LENS. Figure 1e also shows how the ENSO index progresses before and after the June–August ENSO index time period used in this study. Figure 1 shows that when a June–August ENSO event occurs, on average the event begins to strengthen in the early part of the year, and peaks late in the year and into the following year, i.e., peaks in austral summer before diminishing. This is consistent with the three different models and JRA-55, which gives confidence that the models are representing the seasonality of ENSO correctly.

Calculation of the eddy-driven jet stream location was performed by finding the latitude of maximum zonal wind between 70–40°S at 500 hPa. At this pressure level, separation of the eddy-driven and sub-tropical jets was easily performed by restricting the latitude range to these values. Eddy-driven jet stream analysis was also done at 850 hPa to make sure separation between the two jets was accurate. Otherwise, 850 hPa was not used here as much of the Antarctic surface is above this level. The latitude of the eddy-driven jet was smoothed using a moving mean of 20° in longitude.

To separate the influence of the tropospheric and stratospheric pathways of ENSO on tropospheric circulation changes, we first isolate the region where the largest stratospheric

temperature perturbations associated with ENSO are located, i.e. within 60–180°E and 75–45°S at 30 hPa. Then, we identify any El Niño years that correspond to large temperature anomalies within that region of greater or less than 1 or -1 standard deviations during the September-October mean. The same approach is used for La Niña events (See Table S1 for a list of stratospheric response years in JRA-55). This time period, pressure level, and latitude-longitude range was used as it gives the best signal to noise ratio in WACCM and JRA-55. Better results for CanESM2 are obtained when using higher pressure levels, but for consistency, 30 hPa is used. ENSO years that correspond to large Antarctic stratospheric changes are characterized as having a stratospheric response, hereafter referred to as: the combined pathway, and ENSO years that do not correspond to large Antarctic stratospheric changes are characterized as having a passive stratospheric response, hereafter referred to as: tropospheric only pathway. El Niño and La Niña composite anomalies are computed as the difference from the entire climatology. Separating the ENSO events in this way allows for the evaluation of any ENSO stratospheric pathway (difference between combined and tropospheric only pathways) that may affect SH tropospheric circulation. See Table 2 for more information. Significance between subsets of data with and without a stratospheric pathway is shown at the 90th percentile following a two-sided t-test.

4. Results

a. Stratospheric composite differences

The late austral winter and early austral spring ENSO composite differences (El Niño minus La Niña) of stratospheric temperature are shown in Figure 2 for JRA-55, WACCM-GHG$_H$ODS$_H$, LENS, and CanESM2. The high SH latitude composite differences at 10 hPa in August are largely negative and contained mostly within 0–180°E, with smaller positive differences within 180-300°E above the southeastern Pacific (Figure 2a, d, g, and j). For

252 simplicity, here we are showing the composite differences between El Niño and La Niña
253 years, instead of the El Niño and La Niña composite anomalies separately. For the most part,
254 the SH stratospheric response to El Niño and La Niña are similar and opposite (See Figures
255 S1 and S2 for separation into El Niño and La Niña composite anomalies).

256 The largest differences occur in the WACCM-GHG$_H$ODS$_H$ ensemble, of less than -9
257 degrees, which compares to JRA-55 values of up to -7 degrees. The anomalies are weaker in
258 LENS and CanESM2 but the spatial structure of the anomalies is captured very well by all
259 three ensembles. The anomalies are significant at the 95th percentile in the SH in JRA-55 and
260 the different ensembles. The nature of these anomalies arises from both a change in the
261 amplitude and the phase of the zonal wave-1, which is the dominant quasi-stationary wave in
262 the stratosphere during austral spring (e. g. Waugh et al. 1999; Lin et al. 2009). During an El
263 Niño, the zonal wave-1 has a smaller amplitude compared to a La Niña, especially near the
264 wave maximum, and the phase is shifted eastward (See Figure 7).

265 The anomalies descend and move eastward throughout the late winter and spring. During
266 September (Figure 2, b, e, h, and k), there is again excellent agreement of the structure of the
267 anomalies between JRA-55 and the three ensembles, with high SH latitude negative
268 anomalies at 30 hPa now mostly contained within 60–180°E and much smaller positive
269 anomalies within 220–300°E. The differences are now largest in JRA-55, at nearly -9
270 degrees. During October at 100 hPa (Figure 2c, f, i, and l), the anomalies are still present, and
271 significant, in JRA-55, WACCM-GHG$_H$ODS$_H$, and CanESM2 (they are also present in
272 ERA5 reanalysis, but not shown here). However, they are largely reduced in LENS. As an
273 austral winter ENSO event likely precedes an austral summer ENSO event (Figure 1e), and
274 considering that ozone and temperature are strongly coupled in the stratosphere (Randel and
275 Cobb 1994), these results are broadly consistent with the 6 month lag of total column ozone
276 anomalies with ENSO presented in previous literature (Lin and Qian 2019; Evtushevsky et al.

277 2015). The vertical structure of these differences can be seen further in Figure 3, which
278 shows JRA-55 and WACCM-GHG$_H$ODS$_H$ longitude-pressure plots averaged over 45–75°S
279 for individual months from August to November. The negative differences that are associated
280 with El Niño in the lower stratosphere are accompanied by positive differences above. As the
281 differences continue to descend through late spring and summer, these positive differences
282 are found in the middle stratosphere, in agreement with Domeisen et al., (2019), and
283 references therein.

284 The smaller magnitude of the LENS differences in October compared to JRA-55,
285 WACCM-GHG$_H$ODS$_H$ and CanESM2 are most pronounced in the La Niña anomalies (Figure
286 S2), and could be due to either the LENS low top model of ~4 hPa not properly representing
287 the anomalies throughout the upper stratosphere and the mesosphere, or, the prescribed ozone
288 fields damping the anomaly signal during austral spring by having mismatched amplitudes
289 and phases of the temperature and ozone zonal wave-1. This could occur because the
290 temperature field is also influenced by dynamical drivers, such as ENSO. The differences
291 could also be due to LENS having a much larger amplitude of the zonal wave-1 in the
292 Antarctic stratosphere during spring compared to JRA-55, WACCM and CanESM2 (see
293 Figure S3), however, further research is needed.

294 The composite differences seen in Figure 2 for different models are also seen in the three
295 other WACCM ensembles, shown in Figure 4. There are some differences between the
296 ensembles, for example, there is a larger difference (up to -6 K larger) in WACCM-
297 GHG$_H$ODS$_H$ during August at 10 hPa and September at 30 hPa (Figure 4a, and b) compared
298 to the other three ensembles, most noticeably WACCM-GHG$_L$ODS$_H$ (Figure 4g, and h) and
299 WACCM-GHG$_L$ODS$_L$ (Figure 4j, and k), suggesting that the ENSO teleconnection onto the
300 SH stratosphere may be stronger under enhanced GHG loading as these differences do lie

outside the 95th percentile of 1000 sample bootstrapped variability (not shown). However, caution must be taken here as how ENSO and tropospheric ENSO teleconnections respond to different GHGs scenarios are model-dependent (Yeh et al. 2018; Santoso et al. 2019; Cai et al. 2019).

The La Niña composite anomalies are strongest in August at 10 hPa in WACCM-GHG_HODS_H, but are strongest in September at 30 hPa in the other three ensembles, indicating there may be large variability in the timing of the stratospheric teleconnection captured here between ensembles (See Figures S4 and S5). There are also larger differences in WACCM-GHG_HODS_H compared to WACCM-GHG_HODS_L during October at 100 hPa, a time period and pressure level where ozone feedbacks onto temperature perturbations would take place. However, they are less significant.

These differences indicate that forcing changes may alter ENSO teleconnections into the SH stratosphere under different GHG and ODS scenarios. However, for the purposes of this paper, the main take away from Figure 3 is that a SH stratospheric ENSO teleconnection is present, and is broadly consistent within the four different WACCM ensembles. It will therefore likely remain present into the near future as both GHG and ODS concentrations continue to change. Since the teleconnections are similar, later we combine the 4 WACCM ensembles to reduce sampling variability.

Table 2 breaks down, in more detail, the percentage of austral winter El Niño and La Niña events that are associated with a warm or cold Antarctic stratosphere in September–October at 30 hPa within the region of 60°–180°E and 45°–75˚S (above or below one standard deviation). LENS is omitted here due to the weaker stratospheric response to ENSO simulated in this ensemble (see Figure 2). JRA-55 El Niños and La Niñas are associated with a cold or warm Antarctic stratosphere with an incident rate of 42.9% and 41.7% respectively.

In contrast, the opposite, i.e., El Niño associated with a warm stratosphere, does not occur. These results are reflected in the model composites. Across all ensembles and JRA-55, the incident rates of El Niño associated with a warm or cold stratosphere are 6.5% and 30.7% respectively, while the incident rates of La Niña and a warm or cold stratosphere are 23.7% and 8.2%. (See Figure S6 for a scatter plot representation)

In the NH, Butler et al. (2014) showed that a SSW likely occurs during either an El Niño or La Niña winter. Here, in the SH, since SSWs are rare, we follow a different approach and investigate high and low temperature extremes. This produces a clear linear positive or negative temperature response of the stratosphere to the phase of ENSO, i.e., negative during El Niño and positive during La Niña.

The robustness of the August–October stratospheric differences (El Niño minus La Niña) associated with, and likely forced by the onset of ENSO events in the austral winter are seen to be different to a Central Pacific-El Niño response (e.g. Hurwitz et al. 2011), where the Central Pacific-El Niño response is associated with an Antarctic stratospheric temperature anomaly of opposite sign during November–December. Additionally, the downward progression of the anomalies seen in Figure 3 raise the question: do these anomalies influence SH tropospheric circulation during spring and summer? Such a relationship could occur since the differences are present in the lower stratosphere from September–November (see Figure 3), a time period of known stratosphere-troposphere coupling (e. g. Lim et al. 2018), especially in the late spring, where the differences are at the same pressures and during the same time period as anthropogenic springtime Antarctic ozone depletion, which is well known to modulate the SAM in austral summer (e.g. Thompson & Solomon, 2002). To investigate this, first we must establish the tropospheric ENSO teleconnection.

As ENSO events generally have peak strength in austral summer (Trenberth 1997) (Figure 1e), the onset of ENSO events in austral winter is very likely to be followed by ENSO events through to summer. Therefore, it is likely that any spring and summer SH circulation changes in the troposphere associated with the previous winter ENSO could be the result of the tropospheric ENSO teleconnection during spring and summer, and any downward propagation that may occur from the ENSO induced stratospheric anomalies could be hidden in these simultaneous teleconnections.

Additionally, any attempt to separate ENSO events by whether or not they are associated with a perturbed stratosphere may end up separating different subsets of ENSO events that have fundamentally different tropospheric teleconnections, and this may obscure any perceived downwards influence of ENSO associated stratospheric anomalies. In the next sections, we show how JRA-55 and the ensembles represent these tropospheric teleconnections, and present a method for separating the stratospheric and tropospheric pathways of ENSO onto springtime SH tropospheric circulation, while carefully taking into account the above two concerns.

b. ENSO teleconnection onto the austral spring eddy jet

The teleconnections between ENSO variability during June–August and the SH circulation are investigated here in the zonal wind fields. Figure 5 shows the ENSO composite difference during austral spring 500 hPa zonal wind for JRA-55, WACCM-GHG$_H$ODS$_H$, LENS, and CanESM2. The ENSO composite difference in the latitude of maximum zonal wind (used as a proxy for the eddy-driven jet location) is also shown. Similarly, to Figures 2 and 3, here we are showing the composite differences for simplicity. The structure of the separate El Niño and La Niña composite anomalies are mostly opposite and similar. However, the magnitude of the El Niño teleconnection is slightly larger than the

La Niña teleconnection in WACCM-GHG$_H$ODS$_H$ and LENS, but not in CanESM2 and JRA-55. This can be seen in context of the stratospheric pathway in section 4c (see Figures 8-10). During spring (Figure 5), there is good agreement between the differences in JRA-55 and all ensembles. In WACCM-GHG$_H$ODS$_H$, LENS, and CanESM2, it is generally seen that there are positive differences equatorward of the average eddy-driven jet location (dashed black line) between 100–200°E, and negative differences equatorward between 180–300°E. In JRA-55, the composite difference pattern agrees well with the models, however, in the region from 0–180°E, the pattern is now located further south in relation to the average location of the eddy-driven jet. During summer, JRA-55 also agrees very well with the three models, with a similar pattern compared to spring (see Figure S7). Therefore, during the warm phase of ENSO, significant positive differences are seen equatorward of the average eddy-driven jet location within the 100-200°E in the models (0-180°E and the South Atlantic during summer). This indicates stronger westerlies and therefore a more equatorward location of the eddy-driven jet during El Niño. In the Southeast Pacific, significant positive differences are seen poleward of the average eddy-driven jet location in the models and JRA-55, indicating a more poleward location of the eddy-driven jet.

The ENSO composite difference in the eddy-driven jet location is captured in Figure 5e were we see an equatorward shift in the jet between 100–200°E of around 2° latitude, and a poleward shift between 200–300˚E in the models of around 2° latitude. There is reasonable agreement with JRA-55, except between 90–150°E, the jet teleconnection is shifted poleward. In summer (Figure S7), we see an equatorward difference of the jet within 0–180°E of around 1° latitude, with excellent agreement between the models and JRA-55. The peak in the equatorward difference between about 100–200°E where it is up to 2° latitude is the approximate location of the quasi-stationary southwestern Pacific anticyclone (Hobbs and

396 Raphael 2010), and also agrees with Fogt et al. (2012) on regional variations in the SAM
397 associated with ENSO. Further east, over the southeastern Pacific the differences become
398 negative, and are also very strong, up to -2° latitude. This is the location of the quasi-
399 stationary southeastern Pacific anti-cyclone. The differences return to a 0 in the South
400 Atlantic. Therefore, during spring, ENSO is negatively correlated to SAM between 100–
401 200°E and positively correlated between 200–3000°E, as an equatorward shift of the jet
402 would indicate a negative SAM polarity. During the summer (Figure S7) ENSO is negatively
403 correlated to SAM everywhere except the southeastern pacific (200–300°E), in agreement
404 with previous studies (e.g. Fogt et al. 2012; L'Heureux and Thompson 2006; Lim et al.
405 2013). Therefore, it is clear there is regional structure to this correlation, especially in spring.

406 In JRA-55, the zonal wind differences in the SH have become significantly stronger at
407 500 hPa in recent years from 1979 onwards (almost double that of the model simulations),
408 whether this is due to recent years having stronger ENSO events (e.g. Lee and McPhaden
409 2010; Freund et al. 2019), or that there are better observations since 1979 requires further
410 investigation. However, the longitudinal structures of the differences are the same when
411 comparing the ENSO composite differences over 1958–2019 and 1979–2019 (not shown).

412 Figure 6 shows the ENSO composite differences of zonal wind and the eddy-driven jet
413 stream under the different WACCM scenarios for the austral spring period. Since the
414 composite differences are detrended and normalized to the mean, the direct ODS or GHG
415 signal on the eddy-driven jet is removed. Therefore, any significant differences in the ENSO
416 teleconnection between WACCM ensembles will likely arise from either differences in the
417 structure and intensity of ENSO, or non-linearities in how ENSO projects onto SH
418 tropospheric circulation under different GHG or ODS regimes. The zonal wind differences
419 are very similar for the 4 different scenarios indicating that the teleconnection is consistent

for different GHG and ODS loadings during spring. There are some larger differences in summer between scenarios, but they are not consistent when comparing to different CanESM2 ensembles one with only stratospheric ozone forcings, and one with pre-industrial forcings (see Figures S7 and S8). Therefore, the overall longitudinal structure of the teleconnection is very consistent between all models and ensembles, and will therefore likely remain consistent into the near future as GHG and ODS concentrations change. This gives confidence that any stratospheric-tropospheric teleconnection of ENSO onto SH tropospheric circulation will show similar features in all ensembles, and therefore combining the 4 different WACCM ensembles (hereby, referred to as WACCM-combined) to create a larger dataset is a reasonable approach going forward. This has the added benefit of producing a WACCM ensemble with similar ensemble members to CanESM2 (40 members compared to 50 members, respectively).

Here, we have established that the typical ENSO teleconnection onto the tropospheric eddy-driven jet in the SH is not longitudinally uniform in the separate model simulations, in agreement with previous literature (e.g. Fogt et al. 2012). In the next section, we aim to establish whether or not the stratospheric ENSO associated perturbations shown in Figures 2, 3, and 4 exhibit stratosphere-troposphere coupling, thus providing an additional pathway for ENSO to affect SH tropospheric circulation.

c. Downward propagation of ENSO induced stratospheric anomalies

The key obstacle to separating the stratospheric expression of ENSO during austral spring and the tropospheric teleconnection is the strength of the tropospheric teleconnection. We first examine this by separating the austral winter ENSO years that exhibit a stratospheric springtime response in the SH from those that do not. The austral spring stratospheric differences are expected to impact tropospheric circulation as they occur during a key time

period for stratosphere-troposphere coupling (Thompson et al. 2005; Lim et al. 2018). Different metrics of the two subsets of ENSO events are then compared: The stratospheric temperature differences, and the tropical Pacific surface temperature differences. If there are obvious differences in the structure of the surface temperatures (e.g. the location of largest SST differences is located in a different location, or is significantly stronger/weaker), then any differences in the tropospheric wind may just be due to different teleconnections from differing ENSO events. However, if the surface temperature differences are similar, then comparison of the composite anomalies in austral spring tropospheric circulation between these two subsets of data provides an indication of how much the stratospheric ENSO pathway affects tropospheric circulation. If any stratospheric temperature biases existed in the model, they could potentially also affect the stratosphere-troposphere coupling. However, this is unlikely here due to the agreement between JRA-55 and the models in Figures 2-4.

An austral spring stratospheric response to ENSO is characterized here by a large September–October temperature anomaly (greater/less than 1/-1 standard deviations) at 30 hPa within the region of 60–180°E and 75–45°S (i.e., the region of largest anomalies, see Figures 2 and 4). The anomalies are not biased against either an El Niño or La Niña. For example, all El Niño years that have either a positive or negative temperature anomaly exceeding 1 standard deviation within the region are included in the subset of ENSO years with a combined pathway. This ensures that both positive and negative stratospheric extremes are sampled for both phases of ENSO. The remaining years are characterized as ENSO events with a tropospheric only pathway. This methodology is performed for the WACCM-combined and CanESM2 ensembles, and JRA-55. See methods section for more details. The number of coincident El Niño and La Niña years displaying temperature extremes within the

described region are shown in Table 2. The number of stratospheric extremes that occur during neutral ENSO years are also tabulated.

Figure 7 shows the differences between the combined pathway and tropospheric only pathway subsets of ENSO events for WACCM-combined. Figures 7a, and b show September–October temperatures averaged over 75–45°S at 30 hPa. For the tropospheric only pathway (Figure 7a), we see that the El Niño and La Niña years have similar temperatures compared to climatology (black dotted line). While, when there is a combined pathway (Figure 7b), by definition, there is a stratospheric response. Figure 7b shows that the majority of warm temperature anomalies occur during a La Niña, and the majority of cold temperature anomalies occur during an El Niño.

Figures 7c and 7d show the lower stratospheric October temperature responses to the two different subsets of ENSO events. For the tropospheric only pathway, the negative temperature difference that is seen in Figures 2 and 3 all but disappears, and when there is a combined pathway, the negative difference is enhanced. Therefore, when there is a combined pathway, we would expect a circulation response in the troposphere, compared to the tropospheric only pathway, to have similar structure to that of ozone depletion, i.e. a zonal shift in the tropospheric eddy-driven jet (this is investigated in Figures 8-11). To make sure the circulation differences are not due to sampling two subsets of ENSO events that are distinctly different, Figure 7e, and f show the austral spring surface temperature composite differences for the two separate datasets. The figures show that the two different subsets of ENSO events are very similar in structure and intensity and are not significantly different from each other, giving confidence that the difference in the tropospheric composites between the two subsets of data is arising from stratosphere/troposphere coupling. See Figures S10 and S11 for the corresponding figure for JRA-55 and CanESM2.

To establish what the stratospheric extremes shown in Figure 7 would have on the tropospheric circulation during austral spring and summer, Figure 8 shows the 500 hPa zonal wind response to composite warm and cold Antarctic stratospheres that occur during a neutral ENSO year. This is done for JRA-55, CanESM2, and WACCM-combined. Figures 8g, and h show the WACCM difference due to ozone depletion for both austral spring and summer (difference between WACCM-GHG_HODS_H and WACCM-GHG_HODS_L, and includes all ENSO and ENSO-neutral years).

It is clear that when there is a warm Antarctic stratosphere in September–October during an ENSO-neutral year (Figure 8), we see negative 500 hPa zonal wind anomalies near 60°S and positive anomalies near 45°S. This is seen in JRA-55, CanESM2, and WACCM-combined. The opposite is seen when there is a cold Antarctic stratosphere, but they are slightly smaller compared to when there is a warm Antarctic stratosphere. Compared to the anomalies caused by ozone depletion in WACCM during spring (Figure 8g), the anomalies during the cold phase are of similar magnitude and the anomalies during the warm phase are slightly larger. However, comparing to austral summer when the ozone influence on the troposphere is greatest, the anomalies are approximately half during the cold phase and the same during warm phase.

Next, we show the austral spring 500 hPa zonal wind response for the combined pathway, the tropospheric only pathway, and the difference between the two. This is done for the El Niño (Figure 9) and La Niña (Figure 10) composites. Here we have separated El Niño and La Niña, instead of conducting a composite difference, to compare with the neutral ENSO years (Figures 8).

For the JRA-55 El Niño composite during austral spring (Figure 9), the difference (Figure 9c) between the combined pathway (Figure 9a) and tropospheric only pathway (Figure 9b)

515 for 500 hPa zonal wind represents the stratospheric pathway and shows a pattern that is
516 shifted polewards compared to Figure 8b (neutral ENSO with cold stratosphere). Therefore,
517 in this case, we see little agreement with CanESM2 (Figure 9f) and WACCM-combined
518 (Figure 9i), which show positive/negative anomalies south/north of the climatological eddy-
519 driven jet and good agreement with Figures 8c and 8b. This indicates a poleward shift of the
520 eddy-driven jet due to a El Niño associated cold Antarctic stratosphere. It is important to note
521 here that the number of El Niño years available in JRA-55 is a likely reason for any
522 differences between JRA-55 and the model ensembles, which is also clearly seen in the
523 limited significance seen in the JRA-55 composite anomalies (Figure 9a, b) and the
524 differences between the two (Figure 9c). However, for La Niña (Figure 10), the JRA-55 500
525 hPa zonal wind difference (Figure 10c) is very clear and in agreement with both CanESM2
526 (Figure 10f), WACCM-combined (Figure 10i) and Figures 8a, c, and e. WACCM-combined
527 and CanESM2 also show the strongest response during a La Niña, consistent with Figure 8a,
528 c, and e. Therefore, the most significant stratospheric connection of ENSO onto SH
529 circulation is seen during La Niña. This is most notably in austral spring, but it also occurs in
530 austral summer, but the signal is slightly weaker and less significant (See Figures S12 and
531 S13). However, this is expected considering the stratospheric anomalies peak in the early
532 spring.

533 Comparing to figure 8h, we see that the stratospheric pathway of ENSO onto the austral
534 spring zonal wind is approximately half of what is seen due to ozone depletion during austral
535 summer in WACCM for both an El Niño induced cold stratosphere (Figure 9i) and an La
536 Niña induced warm stratosphere (Figure 10i). This brings into context by how much,
537 compared to ozone depletion, an ENSO year that has a stratospheric pathway differs from an
538 ENSO year that doesn't.

Figures 9 and 10 also highlight that the tropospheric pathway (panels b, e, and h) to El Niño and La Niña are not zonally uniform, in agreement with Figures 5 and 6. Meanwhile, the stratospheric pathway (panels c, f, and i) of El Niño and La Niña are more zonally uniform (especially in CanESM2 and WACCM-combined) and opposite to that of the tropospheric pathway between 100–200°E and of the same sign between 200–300°E in austral spring (In austral summer, the stratospheric pathway is opposite everywhere except 200–300°S). Additionally, the stratospheric pathway is slightly weaker compared to the tropospheric pathway in the models. Therefore, even though the stratospheric pathway is clearly present, it is not the major driver of SH ENSO teleconnections in the troposphere, but instead plays a secondary role.

Using large ensembles (50 members for CanESM2, and 40 members for WACCM-combined) allows us to investigate the large variability in the stratospheric pathway on tropospheric circulation. An example of this is shown in Figure 11. Here, significance from a two-sided two-sample t-test for the zonal mean difference at 60°S is shown as a function of the number of ensemble members used. This was calculated by bootstrapping 1000 times the difference between the tropospheric only and combined pathways for different numbers of ensemble members used and taking the average p-value. For La Niña, we need approximately 12 members for WACCM-combined and 22 members for CanESM2 to achieve a zonal average difference that is significant at the 90th percentile. However, for El Niño we need around 35 members for WACCM-combined and 50 members CanESM2 (more regional significance at 60°S requires fewer ensemble members, as can be inferred from Figures 9 and 10). This further indicates that the influence of the stratospheric pathway on tropospheric circulation is stronger and more significant during a La Nina.

5. Conclusions

563 The far-reaching global implications of ENSO have been studied extensively, from
564 impacts on precipitation in Australia and the Americas, to an ENSO stratospheric pathway
565 onto the NH surface. Here, we have presented evidence for a novel connection, an ENSO
566 stratospheric pathway onto SH circulation during the austral summer. The SH teleconnections
567 act as a pathway to the surface through stratosphere/troposphere coupling.

568 We investigate the effects of austral winter ENSO, calculated as the first principle
569 component of Tropical Pacific surface temperatures, on the SH stratosphere with JRA-55
570 reanalysis, and six model ensembles using three different global climate models: CESM1
571 WACCM4, CESM1 LENS, and the CanESM2 models.

572 All model ensembles and JRA-55 display large late austral winter and austral spring
573 stratospheric anomalies associated with austral winter ENSO events. This is defined by large
574 negative composite differences in temperature (El Niño minus La Niña) throughout the high
575 latitude SH stratosphere within 0-180°E, and smaller positive anomalies within 180-300°E, a
576 clear modulation of the zonal wave-1, in agreement with other recent studies (Lin and Qian
577 2019), but in general of opposite sign of the response to a Central Pacific El Niño (e.g.
578 Hurwitz et al. 2011). The differences arise as early as August, peaking around 10 hPa and
579 near 60°S, but extending as low as 100 hPa. Over the following months, the peak differences
580 descend through the stratosphere into the middle and lower polar stratosphere, causing large
581 disturbances of up to -8 K in JRA-55 and -5 K in WACCM, at 100 hPa in October, and
582 causing consistent lower stratospheric differences from August–October, a key time for
583 stratosphere-troposphere coupling. This teleconnection is consistent amongst all model
584 ensembles and JRA-55 in August, September, and October, with the exception of LENS in
585 October, which shows much smaller anomalies in the lower stratosphere. The lack of a
586 consistent signal in LENS as the anomalies descend throughout the spring is likely not due to

587 a low top model or prescribed ozone, since CanESM2 retains the anomalies; it may be due to
588 overly large wave amplitudes in LENS obscuring the signal.

589 Comparison of different WACCM ensembles shows that even though there are some
590 differences in the strength of the signal, it is consistent under different GHG and ODS
591 scenarios, indicating that it will remain into the near future as GHG and ODS concentrations
592 change. There is some evidence that high GHG loading may be acting to enhance the ENSO
593 signal in the SH austral stratosphere, especially during an August El Niño at 10 hPa. It is less
594 clear how high ODS loading modulates the signal, with only small differences seen in
595 October at 100 hPa. However, how ENSO and ENSO teleconnections respond to different
596 GHGs scenarios are model-dependent and have not reached an inter-model consensus (Yeh et
597 al. 2018; Santoso et al. 2019; Cai et al. 2019).

598 The SH austral spring and summer eddy-driven jet locations are linked to ENSO, with an
599 equatorward shift occurring during an El Niño over the 100-200°E and a poleward shift
600 occurring between 200-300°E during spring. During summer the equatorward shifts extend
601 from 0–200°E and the South Atlantic. This indicates that its relationship to the SAM is not
602 zonally symmetric, in agreement with previous work (e,.g. Fogt et al. 2012; Lim et al. 2013).

603 By separating ENSO events that instigate large SH stratospheric temperature anomalies
604 from those that do not and comparing to SH stratospheric temperature anomalies that occur
605 during neutral-ENSO events, we have established that an ENSO stratospheric pathway onto
606 the SH eddy-driven jet exists during austral spring and summer. This result is robust among
607 CanESM2, and in a combination of the WACCM ensembles for both La Niña and El Niño
608 events. JRA-55 reanalysis shows good agreement with the model ensembles for La Niña
609 during spring and summer, but there is an inconsistent response for El Niño events in JRA-55
610 during spring. However, both the WACCM and CanESM2 stratospheric pathways are also

611 most significant during La Niña compared to El Niño, and a large number of ensemble
612 members are needed to obtain significance at the 90th percentile for El Niño events. This is
613 also consistent with the tropospheric response being larger during a neutral-ENSO warm
614 stratosphere compared to a cold stratosphere in JRA-55 and the models (Figure 8).

615 In the NH, Butler et al. (2014) showed that it is common for SSWs to occur during both a
616 La Niña and an El Niño. This teleconnection to the stratosphere results in a different
617 tropospheric response to ENSO due to the downward influence of the SSW in boreal winter,
618 resulting in an ENSO stratospheric pathway to the NH troposphere. The method used here is
619 not directly comparable to Butler et al. (2014), since SSWs are rare in the SH. However, it is
620 clear that an El Niño event has a different impact than a La Niña event in the SH stratosphere.
621 Therefore, the tropospheric expression of the stratospheric anomaly depends largely on the
622 phase of ENSO. An austral winter El Niño will more likely cause a cold, more stable
623 Antarctic stratosphere, which strengthens the spring and summer polar vortex and shifts the
624 jet stream poleward. In contrast, an austral winter La Niña will more likely cause a warm,
625 less stable stratosphere, which weakens the polar vortex and shifts the jet stream
626 equatorward.

627 In addition to what Evtushevsky et al. (2019) reported for austral spring, our results show
628 that when the stratospheric pathway is present, the forcing from the stratospheric anomalies is
629 likely of opposite sign to the tropospheric teleconnection over 100–200°E during spring (0–
630 200°E during summer). This results in a smaller equatorward/poleward shift of the jet stream
631 compared to El Niño/La Niña years that do not have a stratospheric response. The opposite
632 occurs in the southeastern Pacific (200–300°E), where the stratospheric and tropospheric
633 teleconnections are of the same sign, resulting in a larger poleward/equatorward differences
634 of the jet stream in the presence of El Niño/La Niña associated stratospheric anomalies. The

magnitude of the stratospheric pathway is smaller than the tropospheric pathway and is therefore only playing a secondary role in how ENSO affects the tropospheric circulation. For context, the strength of the stratospheric pathway in the models is approximately half of that caused by Antarctic ozone depletion in austral summer. Even though the stratospheric pathway is slightly weaker compared to the tropospheric pathway, it could have meaningful impacts on rainfall and temperature associated with eddy-driven jet driven weather fronts during ENSO events.

Therefore, the stratospheric pathway of ENSO presented here is important for understanding the connection between ENSO and SH circulation anomalies during austral summer, and also for understanding to what extent a particular ENSO event may affect regional climate in the SH.

Acknowledgments.

K.S. and S. S. were supported by a gift to MIT from an anonymous donor and by a grant from the National Science Foundation NSF 1848863. D. W. J. T. is supported by NSF AGS-1848785. This research was enabled by the computational and storage resources of NCAR's Computational and Information Systems Laboratory (CISL), sponsored by the NSF. D. E. K. was partly supported by NSF FESD-1338814. Cheyenne: HPE/SGI ICE XA System (NCAR Community Computing). Boulder, CO: National Center for Atmospheric Research. doi:10.5065/D6RX99HX. We acknowledge Environment and Climate Change Canada's Canadian Centre for Climate Modelling and Analysis for executing and making available the CanESM2 large ensemble simulations, and the Canadian Sea Ice and Snow Evolution (CanSISE) Network for proposing the simulations. The JRA-55 dataset used in this study is from the Japanese 55-year Reanalysis project carried out by the Japan Meteorological Agency (JMA).

Data Availability Statement.

WACCM model results shown in this paper are available online here: https://acomstaff.acom.ucar.edu/dkin/JClim_Stone_2021/. LENS model results are publicly available here: https://www.cesm.ucar.edu/projects/community-projects/LENS/data-sets.html. CanESM2 model results are publicly available here: http://crd-data-donnees-rdc.ec.gc.ca/CCCMA/products/CanSISE/output/CCCma/CanESM2/, JRA-55 data are available here: https://rda.ucar.edu/datasets/ds628.1/.

REFERENCES

Arblaster, J. M., and G. A. Meehl, 2006: Contributions of external forcings to southern annular mode trends. *J. Clim.*, **19**, 2896–2905, https://doi.org/10.1175/JCLI3774.1.

Arora, V. K., and Coauthors, 2011: Carbon emission limits required to satisfy future representative concentration pathways of greenhouse gases. *Geophys. Res. Lett.*, **38**, 3–8, https://doi.org/10.1029/2010GL046270.

Bjerknes, J., 1969: Atmospheric Teleconnections From the Equatorial Pacific 1. *Mon. Weather Rev.*, **97**, 163–172, https://doi.org/10.1175/1520-0493(1969)097<0163:atftep>2.3.co;2.

Butler, A. H., Polvani, and C. Deser, 2014: Separating the stratospheric and tropospheric pathways of El Niño–Southern Oscillation teleconnections. *Environ. Res. Lett.*, **9**, 024014, https://doi.org/10.1088/1748-9326/9/2/024014.

Cai, W., and Coauthors, 2019: Pantropical climate interactions. *Science (80-.).*, **363**, https://doi.org/10.1126/science.aav4236.

Cionni, I., and Coauthors, 2011: Ozone database in support of CMIP5 simulations: Results and corresponding radiative forcing. *Atmos. Chem. Phys.*, **11**, 11267–11292,

https://doi.org/10.5194/acp-11-11267-2011.

Deser, C., I. R. Simpson, K. A. McKinnon, and A. S. Phillips, 2017: The Northern Hemisphere extratropical atmospheric circulation response to ENSO: How well do we know it and how do we evaluate models accordingly? *J. Clim.*, **30**, 5059–5082, https://doi.org/10.1175/JCLI-D-16-0844.1.

Domeisen, D. I. V., C. I. Garfinkel, and A. H. Butler, 2019: The Teleconnection of El Niño Southern Oscillation to the Stratosphere. *Rev. Geophys.*, 5–47, https://doi.org/10.1029/2018RG000596.

Evtushevsky, O. M., V. O. Kravchenko, L. L. Hood, and G. P. Milinevsky, 2015: Teleconnection between the central tropical Pacific and the Antarctic stratosphere: spatial patterns and time lags. *Clim. Dyn.*, **44**, 1841–1855, https://doi.org/10.1007/s00382-014-2375-2.

——, A. V. Grytsai, and G. P. Milinevsky, 2019: Decadal changes in the central tropical Pacific teleconnection to the Southern Hemisphere extratropics. *Clim. Dyn.*, **52**, 4027–4055, https://doi.org/10.1007/s00382-018-4354-5.

Fogt, R. L., D. H. Bromwich, and K. M. Hines, 2011: Understanding the SAM influence on the South Pacific ENSO teleconnection. *Clim. Dyn.*, **36**, 1555–1576, https://doi.org/10.1007/s00382-010-0905-0.

——, J. M. Jones, and J. Renwick, 2012: Seasonal zonal asymmetries in the southern annular mode and their impact on regional temperature anomalies. *J. Clim.*, **25**, 6253–6270, https://doi.org/10.1175/JCLI-D-11-00474.1.

Freund, M. B., B. J. Henley, D. J. Karoly, H. V. McGregor, N. J. Abram, and D. Dommenget, 2019: Higher frequency of Central Pacific El Niño events in recent decades relative to

705 past centuries. *Nat. Geosci.*, **12**, 450–455, https://doi.org/10.1038/s41561-019-0353-3.

706 Fyfe, J. C., and Coauthors, 2017: Large near-Term projected snowpack loss over the western
707 United States. *Nat. Commun.*, **8**, 1–7, https://doi.org/10.1038/ncomms14996.

708 Garreaud, R. D., and D. S. Battisti, 1999: Interannual (ENSO) and interdecadal (ENSO-like)
709 variability in the Southern Hemisphere tropospheric circulation. *J. Clim.*, **12**, 2113–
710 2123, https://doi.org/10.1175/1520-0442(1999)012<2113:IEAIEL>2.0.CO;2.

711 Gong, D., and S. Wang, 1999: Definition of Antarctic Oscillation index. *Geophys. Res. Lett.*,
712 **26**, 459–462, https://doi.org/10.1029/1999GL900003.

713 Grimm, A. M., and R. G. Tedeschi, 2009: ENSO and extreme rainfall events in South
714 America. *J. Clim.*, **22**, 1589–1609, https://doi.org/10.1175/2008JCLI2429.1.

715 Hartmann, D. L., and F. Lo, 1998: Wave-driven zonal flow vacillation in the Southern
716 Hemisphere. *J. Atmos. Sci.*, **55**, 1303–1315, https://doi.org/10.1175/1520-
717 0469(1998)055<1303:WDZFVI>2.0.CO;2.

718 Hobbs, W. R., and M. N. Raphael, 2010: Characterizing the zonally asymmetric component
719 of the SH circulation. *Clim. Dyn.*, **35**, 859–873, https://doi.org/10.1007/s00382-009-
720 0663-z.

721 Horel, J. D., and J. M. Wallace, 1981: Planetary-Scale Atmospheric Phenomena Associated
722 with the Southern Oscillation. *Mon. Weather Rev.*, **109**, 813–829,
723 https://doi.org/https://doi.org/10.1175/1520-0493(1981)109<0813:PSAPAW>2.0.CO;2.

724 Hurrell, J. W., and Coauthors, 2013: The community earth system model: A framework for
725 collaborative research. *Bull. Am. Meteorol. Soc.*, **94**, 1339–1360,
726 https://doi.org/10.1175/BAMS-D-12-00121.1.

727 Hurwitz, M. M., P. A. Newman, L. D. Oman, and A. M. Molod, 2011: Response of the

antarctic stratosphere to two types of el niño events. *J. Atmos. Sci.*, **68**, 812–822, https://doi.org/10.1175/2011JAS3606.1.

Irving, D., and I. Simmonds, 2016: A New Method for Identifying the Pacific – South American Pattern and Its Influence on Regional Climate Variability. *J. Clim.*, 6109–6125, https://doi.org/10.1175/JCLI-D-15-0843.1.

Jiménez-Esteve, B., and D. I. V. Domeisen, 2018: The tropospheric pathway of the ENSO-North Atlantic teleconnection. *J. Clim.*, **31**, 4563–4584, https://doi.org/10.1175/JCLI-D-17-0716.1.

——, and ——, 2020: Nonlinearity in the tropospheric pathway of ENSO to the North Atlantic. *Weather Clim. Dyn.*, **1**, 225–245, https://doi.org/10.5194/wcd-1-225-2020.

Karoly, D. J., 1988: Southern Hemisphere Circulation Features Associated with El Nino Souther Oscilaltion Events. *J. Clim.*, **2**, 1239–1252, https://doi.org/https://doi.org/10.1175/1520-0442(1989)002<1239:SHCFAW>2.0.CO;2.

——, 1990: The role of transient eddies in low-frequency zonal variations of the Southern Hemisphere circulation. *Tellus*, **42A**, 41–50, https://doi.org/https://doi.org/10.1034/j.1600-0870.1990.00005.x.

Kay, J. E., and Coauthors, 2015: The community earth system model (CESM) large ensemble project : A community resource for studying climate change in the presence of internal climate variability. *Bull. Am. Meteorol. Soc.*, **96**, 1333–1349, https://doi.org/10.1175/BAMS-D-13-00255.1.

Kidson, J. W., 1988: Indices of the Southern Hemisphere Zonal Wind. *J. Clim.*, **1**, 183–194.

——, and M. R. Sinclair, 1995: The Influence of Persistent Anomalies on Southern Hemisphere Storm Tracks. *J. Clim.*, **8**, 1938–1950,

https://doi.org/https://doi.org/10.1175/1520-0442(1995)008<1938:TIOPAO>2.0.CO;2.

Kim, B. M., H. Choi, S. J. Kim, and W. Choi, 2017: Amplitude-dependent relationship between the Southern Annular Mode and the El Niño Southern Oscillation in austral summer. *Asia-Pacific J. Atmos. Sci.*, **53**, 85–100, https://doi.org/10.1007/s13143-017-0007-6.

King, A. D., M. G. Donat, L. V. Alexander, and D. J. Karoly, 2015: The ENSO-Australian rainfall teleconnection in reanalysis and CMIP5. *Clim. Dyn.*, **44**, 2623–2635, https://doi.org/10.1007/s00382-014-2159-8.

Kinnison, D. E., and Coauthors, 2007: Sensitivity of chemical tracers to meteorological parameters in the MOZART-3 chemical transport model. *J. Geophys. Res. Atmos.*, **112**, D20302, https://doi.org/10.1029/2006JD007879.

Kobayashi, S., and Coauthors, 2015: The JRA-55 reanalysis: General specifications and basic characteristics. *J. Meteorol. Soc. Japan*, **93**, 5–48, https://doi.org/10.2151/jmsj.2015-001.

L'Heureux, M. L., and D. W. J. Thompson, 2006: Observed relationships between the El-Niño-Southern oscillation and the extratropical zonal-mean circulation. *J. Clim.*, **19**, 276–287, https://doi.org/10.1175/JCLI3617.1.

Lee, T., and M. J. McPhaden, 2010: Increasing intensity of El Niño in the central-equatorial Pacific. *Geophys. Res. Lett.*, **37**, 1–5, https://doi.org/10.1029/2010GL044007.

Lim, E. P., H. H. Hendon, and H. Rashid, 2013: Seasonal predictability of the southern annular mode due to its association with ENSO. *J. Clim.*, **26**, 8037–8054, https://doi.org/10.1175/JCLI-D-13-00006.1.

Lim, E. P., H. H. Hendon, and D. W. J. Thompson, 2018: Seasonal Evolution of

774 Stratosphere-Troposphere Coupling in the Southern Hemisphere and Implications for
775 the Predictability of Surface Climate. *J. Geophys. Res. Atmos.*, **123**, 12,002-12,016,
776 https://doi.org/10.1029/2018JD029321.

777 Lin, J., and T. Qian, 2019: Impacts of the ENSO Lifecycle on Stratospheric Ozone and
778 Temperature. *Geophys. Res. Lett.*, **46**, 10646–10658,
779 https://doi.org/10.1029/2019GL083697.

780 Lin, P., Q. Fu, S. Solomon, and J. M. Wallace, 2009: Temperature trend patterns in Southern
781 Hemisphere high latitudes: Novel indicators of stratospheric change. *J. Clim.*, **22**, 6325–
782 6341, https://doi.org/10.1175/2009JCLI2971.1.

783 Lindzen, R. S., and S. Nigam, 1987: On the role of sea surface temperature gradients in
784 forcing low-level winds and convergence in the Tropics. *J. Atmos. Sci.*, **44**, 2418–2436,
785 https://doi.org/https://doi.org/10.1175/1520-0469(1987)044<2418:OTROSS>2.0.CO;2.

786 Liu, Z., and M. Alexander, 2007: Atmospheric bridge, oceanic tunnel, and global climatic
787 teleconnections. *Rev. Geophys.*, **45**, 1–34, https://doi.org/10.1029/2005RG000172.

788 McBride, J. L., and N. Nicholls, 1983: Seasonal Relationships beween Australian Rainfall
789 and the Southern Oscillation. *Mon. Weather Rev.*, **111**, 1998–2004,
790 https://doi.org/https://doi.org/10.1175/1520-0493(1983)111<1998:SRBARA>2.0.CO;2.

791 McIntyre, M. E., and N. T. Palmer, 1983: Breaking planetary waves in the stratosphere.
792 *Nature*, **305**, 593–600, https://doi.org/https://doi-
793 org.libproxy.mit.edu/10.1038/305593a0.

794 Meinshausen, M., and Coauthors, 2011: The RCP greenhouse gas concentrations and their
795 extensions from 1765 to 2300. *Clim. Change*, **109**, 213–241,
796 https://doi.org/10.1007/s10584-011-0156-z.

Mills, M. J., and Coauthors, 2016: Global volcanic aerosol properties derived from emissions, 1990-2014, using CESM1(WACCM). *J. Geophys. Res. Atmos.*, **121**, 2332–2348, https://doi.org/10.1002/2015JD024290.

Mo, K. C., and G. H. White, 1985: Teleconnections in the Southern Hemisphere. *Mon. Weather Rev.*, **113**, 22–37, https://doi.org/https://doi.org/10.1175/1520-0493(1985)113<0022:TITSH>2.0.CO;2.

——, and G. Ghil, 1987: Statistics and Dynamics of Persistent Anomalies. *J. Atmos. Sci.*, **44**, 877–902, https://doi.org/https://doi.org/10.1175/1520-0469(1987)044<0877:SADOPA>2.0.CO;2.

——, and J. N. Paegle, 2001: The Pacific-South American modes their downstream affects. *Int. J. Climatol.*, **21**, 1211–1229, https://doi.org/10.1002/joc.685.

Neely, R. R. I., and A. Schmidt, 2016: VolcanEESM: Global volcanic sulphur dioxide (SO2) emissions database from 1850 to present—Version 1.0. *Cent. Environ. Data Anal.*, https://doi.org/https://doi.org/10.5285/76ebdc0b-0eed-4f70-b89e-55e606bcd568.

Polvani, L. M., D. W. Waugh, G. J. P. Correa, and S. W. Son, 2011: Stratospheric ozone depletion: The main driver of twentieth-century atmospheric circulation changes in the Southern Hemisphere. *J. Clim.*, **24**, 795–812, https://doi.org/10.1175/2010JCLI3772.1.

Randel, W. J., and J. B. Cobb, 1994: Coherent variations of monthly mean total ozone and lower stratospheric temperature. *J. Geophys. Res.*, **99**, 5433–5447, https://doi.org/10.1029/93JD03454.

Rasmusson, E. M., and T. H. Carpenter, 1982: Variations in Tropical Sea Surface Temperature and Surface Wind Fields Associated with Southern Oscillation/El Niño. *Mon. Weather Rev.*, **110**, 354–384, https://doi.org/https://doi.org/10.1175/1520-

820 0493(1982)110<0354:VITSST>2.0.CO;2.

821 Renwick, J. A., 1998: ENSO-related variability in the frequency of South Pacific blocking.
822 *Mon. Weather Rev.*, **126**, 3117–3123, https://doi.org/10.1175/1520-
823 0493(1998)126<3117:ERVITF>2.0.CO;2.

824 ——, and M. J. Revell, 1999: Blocking over the South Pacific and Rossby wave propagation.
825 *Mon. Weather Rev.*, **127**, 2233–2247, https://doi.org/10.1175/1520-
826 0493(1999)127<2233:BOTSPA>2.0.CO;2.

827 Rogers, J. C., and H. van Loon, 1982: Spatial Variability of Sea Level Pressure and 500 mb
828 Height Anomalies over the Southern Hemisphere. *Mon. Weather Rev.*, **110**, 1375–1392,
829 https://doi.org/https://doi.org/10.1175/1520-0493(1982)110<1375:SVOSLP>2.0.CO;2.

830 Ropelewski, C. F., and M. S. Halpert, 1986: North American precipitation and temperature
831 patterns associated with the El Niño/Southern Oscillation (ENSO). *Mon. Weather Rev.*,
832 **114**, 2352–2362, https://doi.org/10.16309/j.cnki.issn.1007-1776.2003.03.004.

833 Santoso, A., and Coauthors, 2019: Dynamics and predictability of El Niño-Southern
834 oscillation: An Australian perspective on progress and challenges. *Bull. Am. Meteorol.*
835 *Soc.*, **100**, 403–420, https://doi.org/10.1175/BAMS-D-18-0057.1.

836 Seager, R., N. Harnik, Y. Kushnir, W. Robinson, and J. Miller, 2003: Mechanisms of
837 hemispherically symmetric climate variability. *J. Clim.*, **16**, 2960–2978,
838 https://doi.org/10.1175/1520-0442(2003)016<2960:MOHSCV>2.0.CO;2.

839 Simpson, I. R., T. G. Shepherd, and M. Sigmond, 2011: Dynamics of the lower stratospheric
840 circulation response to ENSO. *J. Atmos. Sci.*, **68**, 2537–2556,
841 https://doi.org/10.1175/JAS-D-11-05.1.

842 Solomon, S., D. Kinnison, J. Bandoro, and R. Garcia, 2015: Simulation of polar ozone

depletion: An update. *J. Geophys. Res.*, **120**, 7958–7974, https://doi.org/10.1002/2015JD023365.

——, D. J. Ivy, D. Kinnison, M. J. Mills, R. R. Neely, and A. Schmidt, 2016: Emergence of healing in the Antarctic ozone layer. *Science (80-.).*, **310**, 307–310, https://doi.org/10.1126/science.aae0061.

——, and Coauthors, 2017: Mirrored changes in Antarctic ozone and stratospheric temperature in the late 20th versus early 21st centuries. *J. Geophys. Res. Atmos.*, **122**, 8940–8950, https://doi.org/10.1002/2017JD026719.

Son, S. W., N. F. Tandon, L. M. Polvani, and D. W. Waugh, 2009: Ozone hole and Southern Hemisphere climate change. *Geophys. Res. Lett.*, **36**, 3–7, https://doi.org/10.1029/2009GL038671.

Stone, K. A., S. Solomon, and D. E. Kinnison, 2018: On the Identification of Ozone Recovery. *Geophys. Res. Lett.*, **45**, https://doi.org/10.1029/2018GL077955.

Szeredi, I., and D. J. Karoly, 1987: The horizontal structure of monthly fluctuations of the Southern Hemisphere troposphere from station data. *Aust. Meteorol. Mag.*, **35**, 119–129, https://doi.org/http://www.bom.gov.au/jshess/docs/1987/szeredi2.pdf.

Thompson, D. W. J., and J. M. Wallace, 2000: Annular Mode in the Extratropical Circulation. Part I : Month-to-Month Variability. *J. Clim.*, **13**, 1000–1016, https://doi.org/http://dx.doi.org/10.1175/1520-0442(2000)013<1000:AMITEC>2.0.CO;2.

Thompson, D. W. J., and S. Solomon, 2002: Interpretation of Recent Southern Hemisphere Climate Change. *Science (80-.).*, **296**, 895–899, https://doi.org/10.1126/science.1069270.

866 Thompson, D. W. J., S. Solomon, and M. P. Baldwin, 2005: Stratosphere – Troposphere
867 Coupling in the Southern Hemisphere. *J. Atmos. Sci.*, **52**, 708–715,
868 https://doi.org/https://doi.org/10.1175/JAS-3321.1.

869 Thompson, D. W. J., S. Solomon, P. J. Kushner, M. H. England, K. M. Grise, and D. J.
870 Karoly, 2011: Signatures of the Antarctic ozone hole in Southern Hemisphere surface
871 climate change. *Nat. Geosci.*, **4**, 741–749, https://doi.org/10.1038/ngeo1296.

872 Trenberth, K. E., 1984: Signal Versus Noise in the Southern Oscillation. *Mon. Weather Rev.*,
873 **1112**, 326–332, https://doi.org/https://doi.org/10.1175/1520-
874 0493(1984)112<0326:SVNITS>2.0.CO;2.

875 ——, 1997: The Definition of El Niño. *Bull. Am. Meteorol. Soc.*, **78**, 2771–2777,
876 https://doi.org/10.1175/1520-0477(1997)078<2771:TDOENO>2.0.CO;2.

877 Wang, L., P. J. Kushner, and D. W. Waugh, 2013: Southern hemisphere stationary wave
878 response to changes of ozone and greenhouse gases. *J. Clim.*, **26**, 10205–10217,
879 https://doi.org/10.1175/JCLI-D-13-00160.1.

880 Waugh, D. W., W. J. Randel, S. Pawson, P. A. Newman, and E. R. Nash, 1999: Persistence
881 of the lower stratospheric polar vortices. *J. Geophys. Res. Atmos.*, **104**, 27191–27201,
882 https://doi.org/10.1029/1999JD900795.

883 WMO, 2011: Scientific Assessment of Ozone Depletion: 2010. *Glob. Ozone Res. Monit.*
884 *Proj. No. 52*, 516.

885 Wyrtki, K., 1975: El Niño—The Dynamic Response of the Equatorial Pacific Ocean to
886 Atmospheric Forcing. *J. Phys. Oceanogr.*, **5**, 285–299,
887 https://doi.org/https://doi.org/10.1175/1520-0485(1975)005<0572:ENTDRO>2.0.CO;2.

888 Yang, C., T. Li, X. Dou, and X. Xue, 2015: Signal of central Pacific El Niño in the Southern

889 Hemispheric stratosphere during austral spring. *J. Geophys. Res.*, **120**, 11438–11450,
890 https://doi.org/10.1038/175238c0.

891 Yeh, S. W., and Coauthors, 2018: ENSO Atmospheric Teleconnections and Their Response
892 to Greenhouse Gas Forcing. *Rev. Geophys.*, **56**, 185–206,
893 https://doi.org/10.1002/2017RG000568.

894

895 TABLES

896 **Table 1. Description of model ensembles and their forcings.**

Model	Ensemble name	No. members	Time period used	GHGs	ODSs/Ozone fields	Ocean	Model top
CESM1-WACCM(CAM4)	**WACCM-GHG_HODS_H**	10	1995–2024	RCP 6.0 after 2005 (Meinshausen et al. 2011)	(WMO 2011)	POP2	66 levels with a top at $5.1x10^{-6}$ hPa
CESM1-WACCM(CAM4)	**WACCM-GHG_LODS_L**	10	1955–1979	Historical	Historical	POP2	66 levels with a top at $5.1x10^{-6}$ hPa
CESM1-WACCM(CAM4)	**WACCM-GHG_LODS_H**	10	1995–2024	Fixed 1960 levels	(WMO 2011)	POP2	66 levels with a top at $5.1x10^{-6}$ hPa
CESM1-WACCM(CAM4)	**WACCM GHG_HODS_L**	10	1995–2024	RCP 6.0 after 2005 (Meinshausen et al. 2011)	Fixed 1960 levels	POP2	66 levels with a top at $5.1x10^{-6}$ hPa
CESM1(CAM5)	**LENS**	40	1995–2024	RCP 8.5 after 2005 (Meinshausen et al. 2011)	Prescribed zonally 4D fields from CESM1(WACCM) CMIP runs with a 10-year running mean. See Kay et al., (2015a) for details.	POP2	30 levels with a top at 3.64 hPa
CanESM2	**CanESM2**	50	1995–2024	RCP 8.5 after 2005, (Meinshausen et al. 2011)	Prescribed zonally symmetric ozone fields from modified SPARC dataset (Cionni et al. 2011)	NCOM 1.3 (Hurrell et al. 2013)	22 levels with a top at 1 hPa

897

898 **Table 2. Number of June–August El Niños and La Niñas that correspond to a warm or**

899 **cold stratosphere within the region of 60°–180°E and 45°–75˚S at 30 hPa during**

900 **September and October.**

	No. El Niños	No. La Niñas	No. El Niños and warm stratosphere	No. El Niños and cold stratosphere	No. La Niñas and warm stratosphere	No. La Niñas and cold stratosphere	No. neutral ENSO	No. warm stratosphere and neutral ENSO	No. cold stratosphere and neutral ENSO
JRA-55	7	12	0	3 (42.9%)	5 (41.7%)	0	43	8 (18.6%)	7 (16.3%)
WACCM-GHG$_H$ODS$_H$	51	49	2 (3.9%)	21 (41.2%)	11 (22.4%)	2 (4.1%)	200	38 (19.0%)	25 (12.5%)
WACCM-GHG$_H$ODS$_L$	47	45	2 (4.3%)	16 (34.0%)	10 (22.2%)	4 (8.9%)	208	35 (16.8%)	30 (14.4%)
WACCM-GHG$_L$ODS$_H$	56	50	1 (1.8%)	13 (23.2%)	13 (26.0%)	7 (14.0%)	194	25 (12.9%)	40 (20.1%)
WACCM-GHG$_L$ODS$_L$	44	42	2 (4.5%)	14 (31.8%)	8 (19.0%)	3 (7%)	164	30 (18.3%)	24 (14.6%)
CanESM2	222	240	21 (9.5%)	64 (28.8%)	57 (23.4%)	20 (8.3%)	1038	162 (15.6%)	139 (13.4%)
WACCM-combined	198	186	7 (3.5%)	64 (32.3%)	42 (22.6%)	16 (8.6%)	766	128 (16.75)	119 (15.5%)
All	427	438	28 (6.5%)	131 (30.7%)	104 (23.7%)	36 (8.2%)	1847	298 (16.1%)	265 (14.4%)

901

902

903

904 FIGURES

905

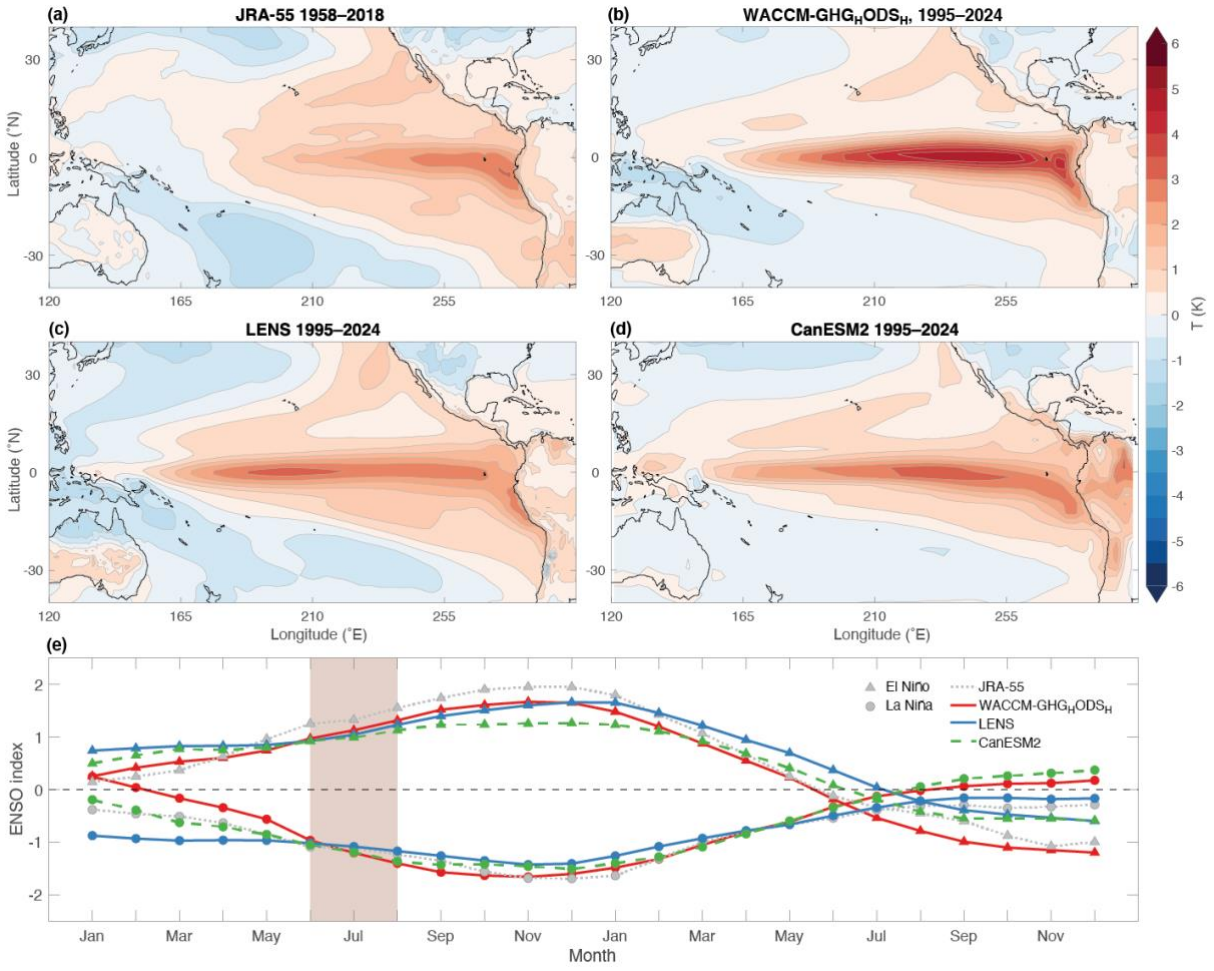

906

907 **Figure 1**. June-August ENSO composite differences (El Niño - La Niña) of June–August
908 surface temperatures for (a) JRA-55, (b) WACCM-GHG$_H$ODS$_H$, (c) LENS, and (d),
909 CanESM2. The seasonality of a June-August ENSO event is shown in (e). The shaded region
910 indicates the months that were used in the construction of the seasonal ENSO index in this
911 paper.

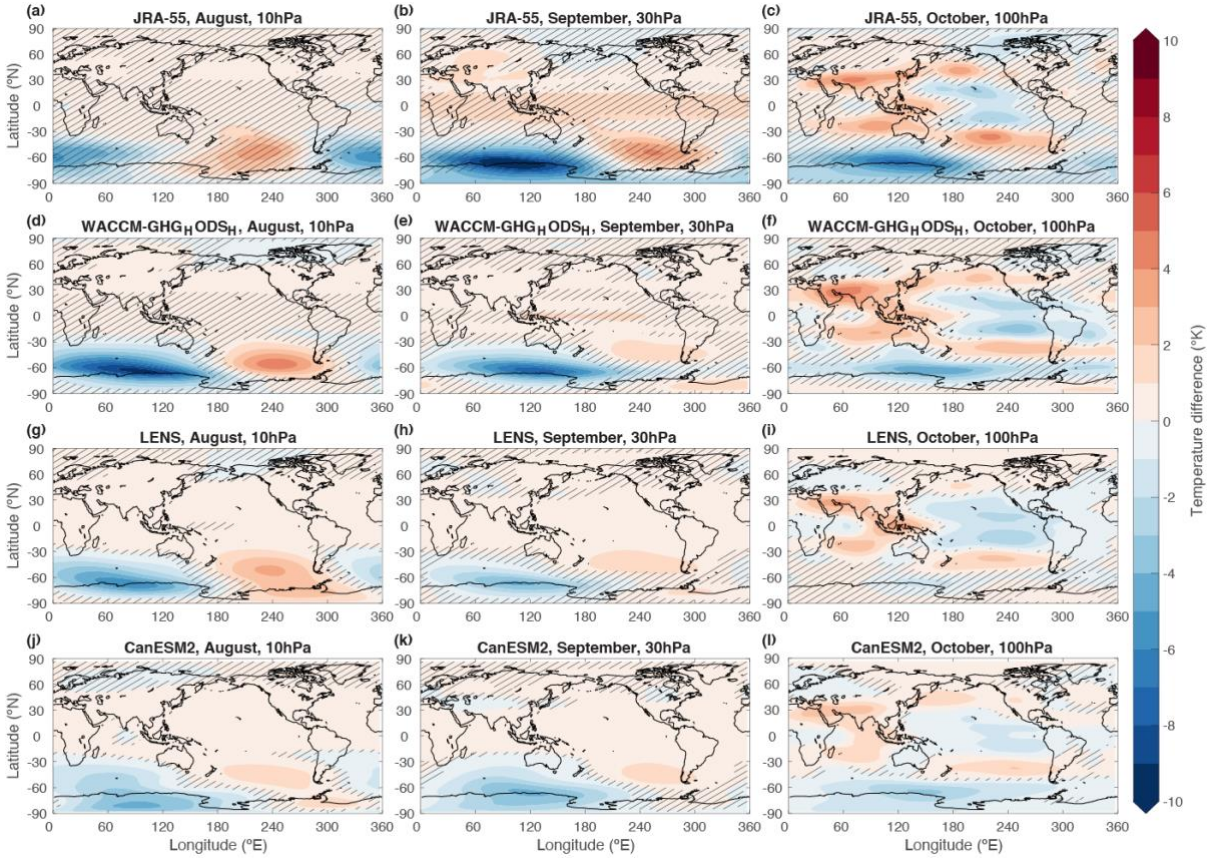

912

913 **Figure 2.** June–August ENSO composite differences of August 10 hPa, September 30 hPa,
914 and October 100 hPa temperatures for JRA-55 (a, b, c), WACCM-GHG$_H$ODS$_H$ (d, e, f),
915 LENS (g, h, i), and CanESM2 (j, k, l). Hatching shows where differences are not significantly
916 different from each other ($p < .05$) using a two-tailed t-test.

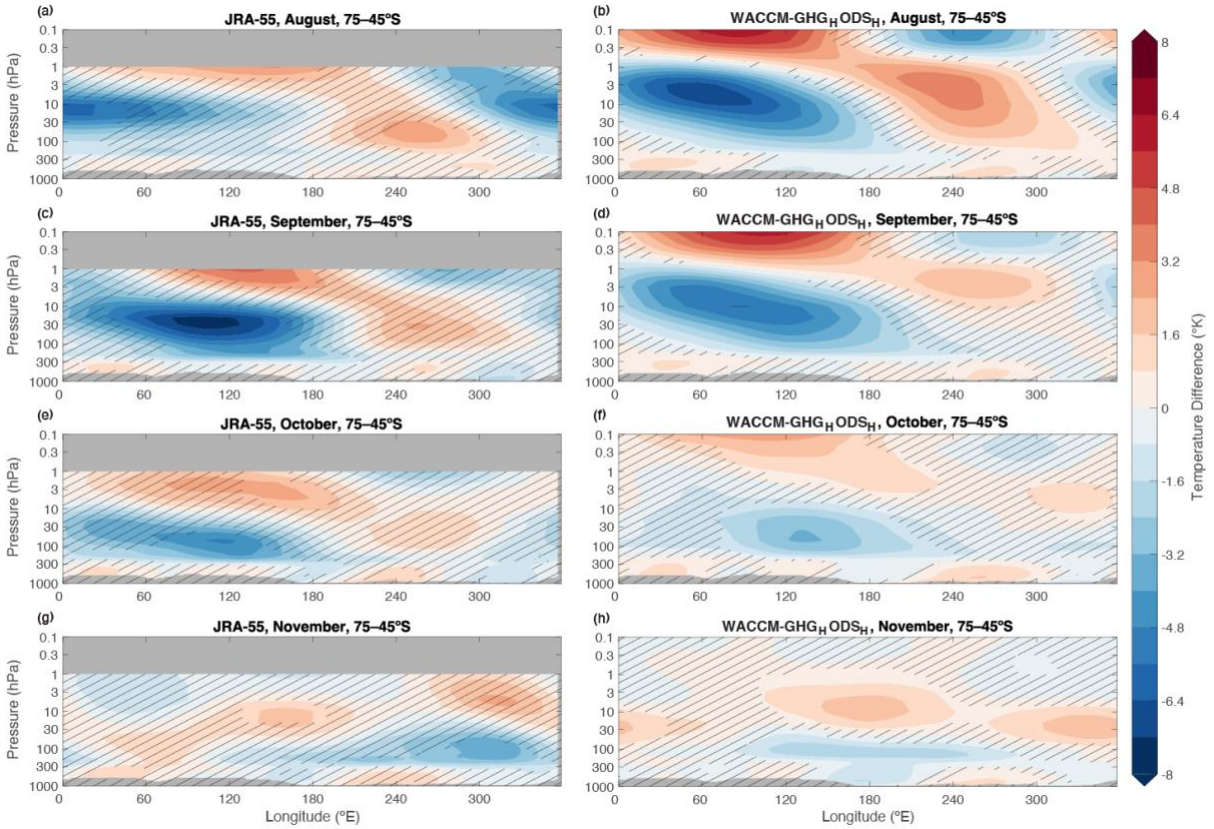

Figure 3. Longitude-Pressure ENSO composite differences of temperature for JRA-55 (left panels) and WACCM-GHG$_H$ODS$_H$ (right panels) averaged over 45–75°S. Four rows show results for August, September, October, and November. Hatching shows where differences are not significantly different from each other ($p < .05$) using a two-tailed t-test.

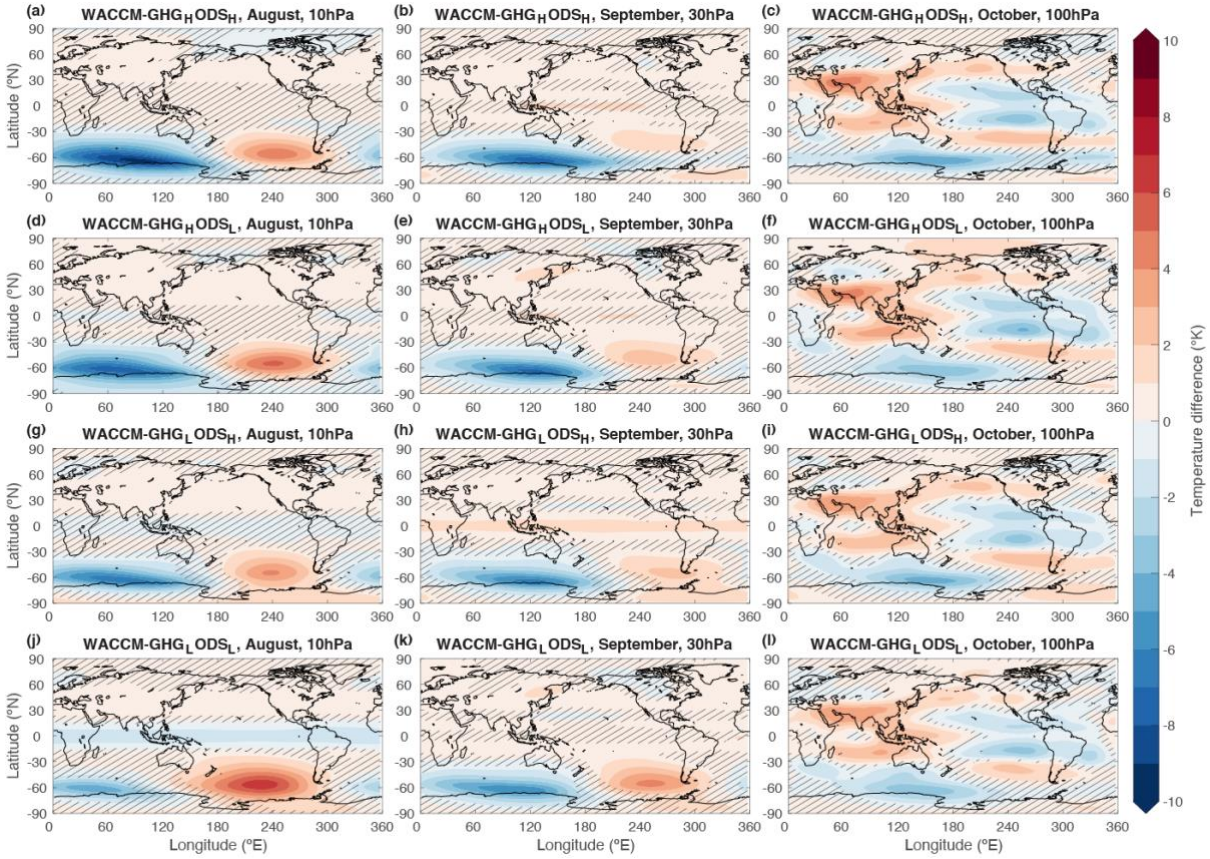

922

923 **Figure 4.** June–August ENSO composite differences of August 10 hPa, September 30 hPa,
924 and October 100 hPa temperatures for WACCM-GHG$_H$ODS$_H$ (a, b, c), WACCM-
925 GHG$_H$ODS$_L$ (d, e, f), WACCM-GHG$_L$ODS$_H$ (g, h, i), and WACCM-GHG$_L$ODS$_L$ (j, k, l).
926 Hatching shows where differences are not significantly different from each other ($p < .05$)
927 using a two-tailed t-test.

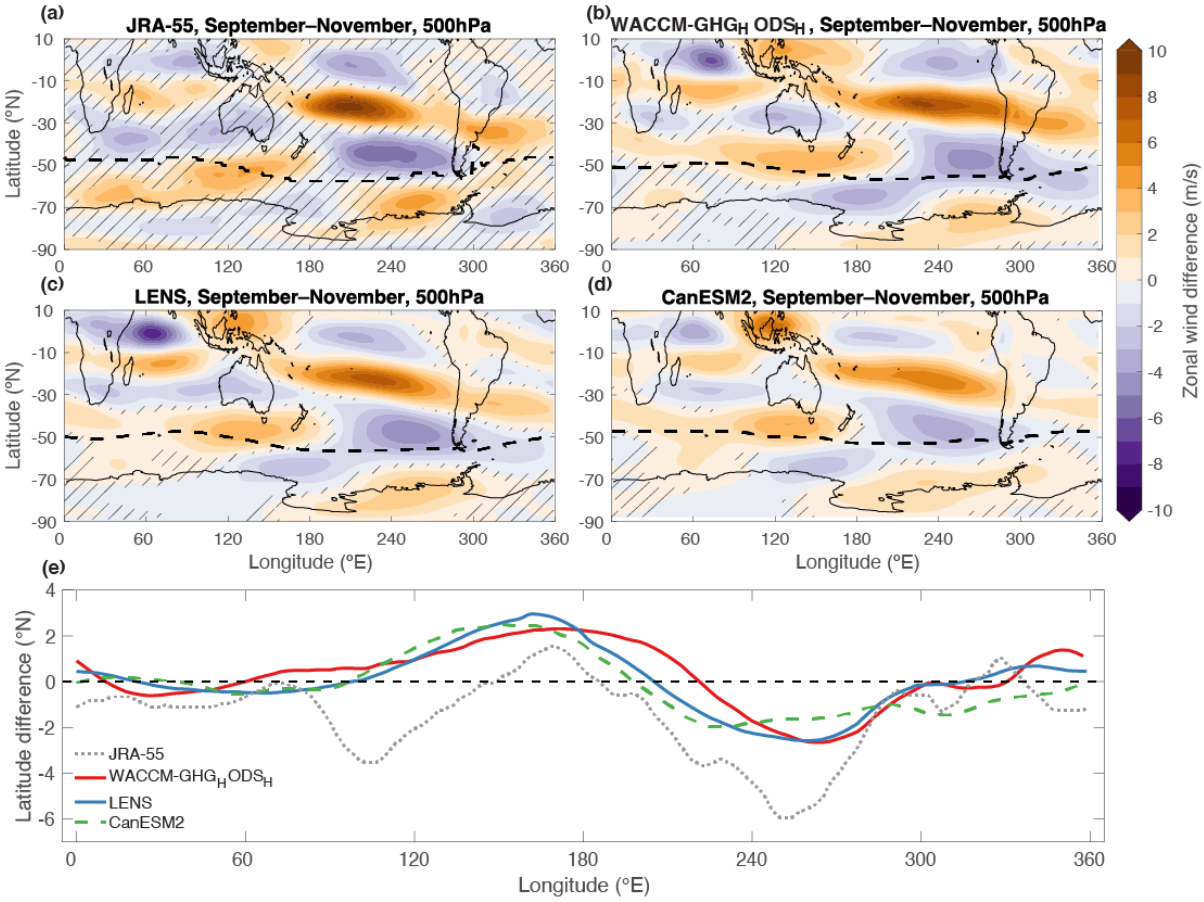

928

929 **Figure 5.** June–August ENSO composite differences of September–November 500 hPa zonal
930 wind for (a) JRA-55, (b) WACCM-GHG$_H$ODS$_H$, (c) LENS, and (d) CanESM2. Dashed black
931 lines indicate the latitudes of maximum zonal wind. Hatching shows where differences are
932 not significantly different from each other ($p < .1$) using a two-tailed t-test. The ENSO
933 composite difference of the latitudes of maximum zonal wind are shown as a function of
934 longitude in (e).

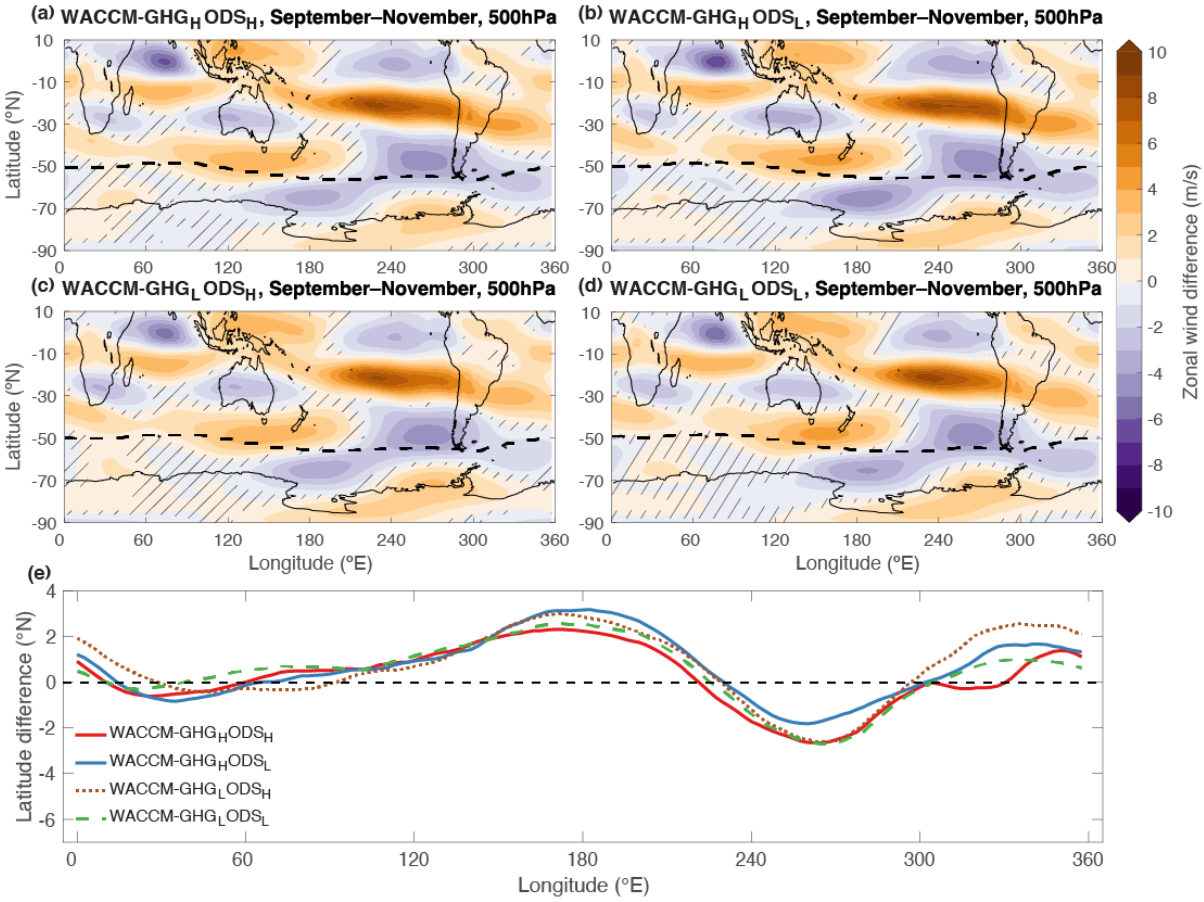

935

936 **Figure 6.** June–August ENSO composite differences of September–November 500 hPa zonal
937 wind for (a) WACCM-GHG$_H$ODS$_H$, (b) WACCM-GHG$_H$ODS$_L$, (c) WACCM-GHG$_L$ODS$_H$,
938 and (d) WACCM-GHG$_L$ODS$_L$. Dashed lines indicate the latitudes of maximum zonal wind.
939 Hatching shows where differences are not significantly different from each other ($p < .1$)
940 using a two-tailed t-test. The ENSO composite difference of the latitudes of maximum zonal
941 wind as a function of longitude are shown in (e).

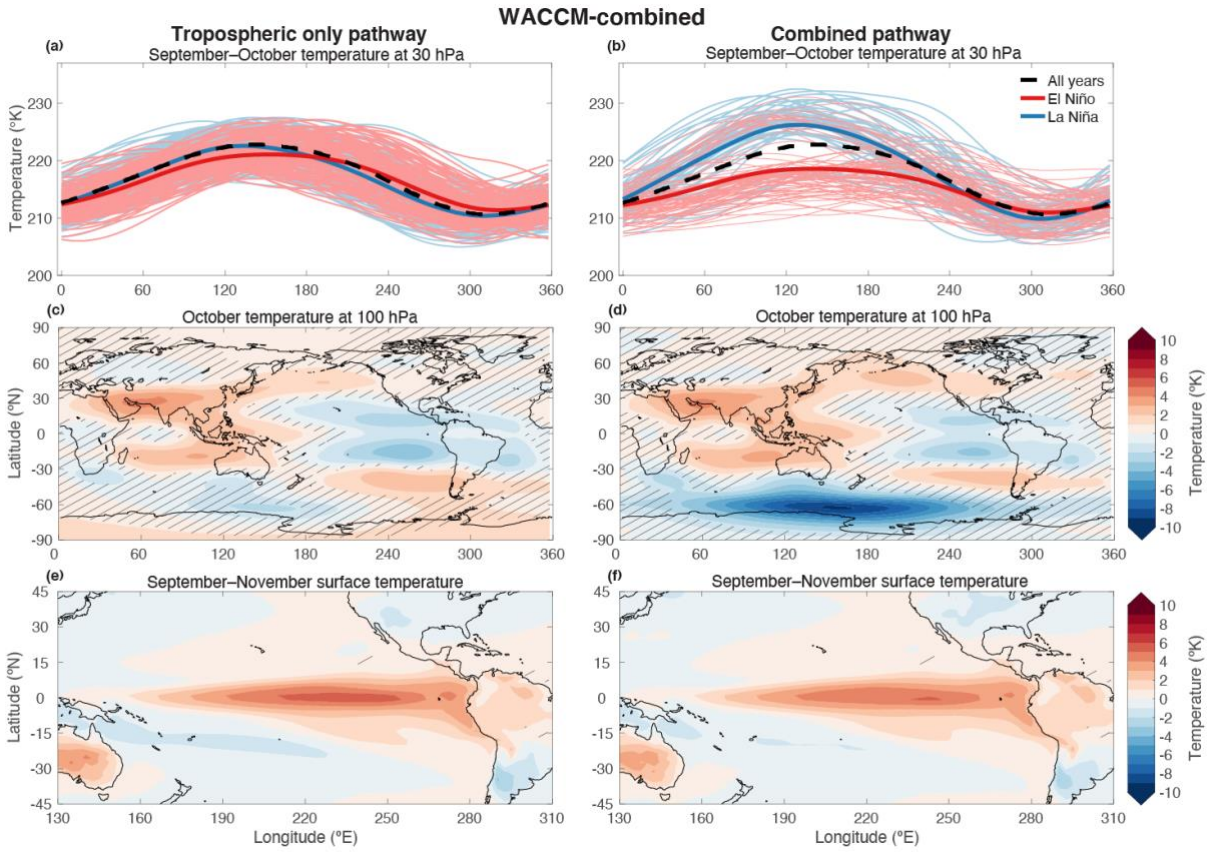

942

943 **Figure 7.** Separation of June–August ENSO events that have an austral spring stratospheric
944 response between 75–45°S and 60–180°E (b) and those that do not (a) in WACCM-
945 GHG$_H$ODS$_H$. The ENSO composite differences of October 100 hPa temperatures are shown
946 for the two subsets of ENSO years (c and d). Similarly September–November surface
947 temperature (e and f). For (a-d), hatching shows where differences are not significantly
948 different from each other ($p < .1$) using a two-tailed t-test. For (e and f), hatching shows
949 where the composite differences in (e) are significantly different from (f).

950

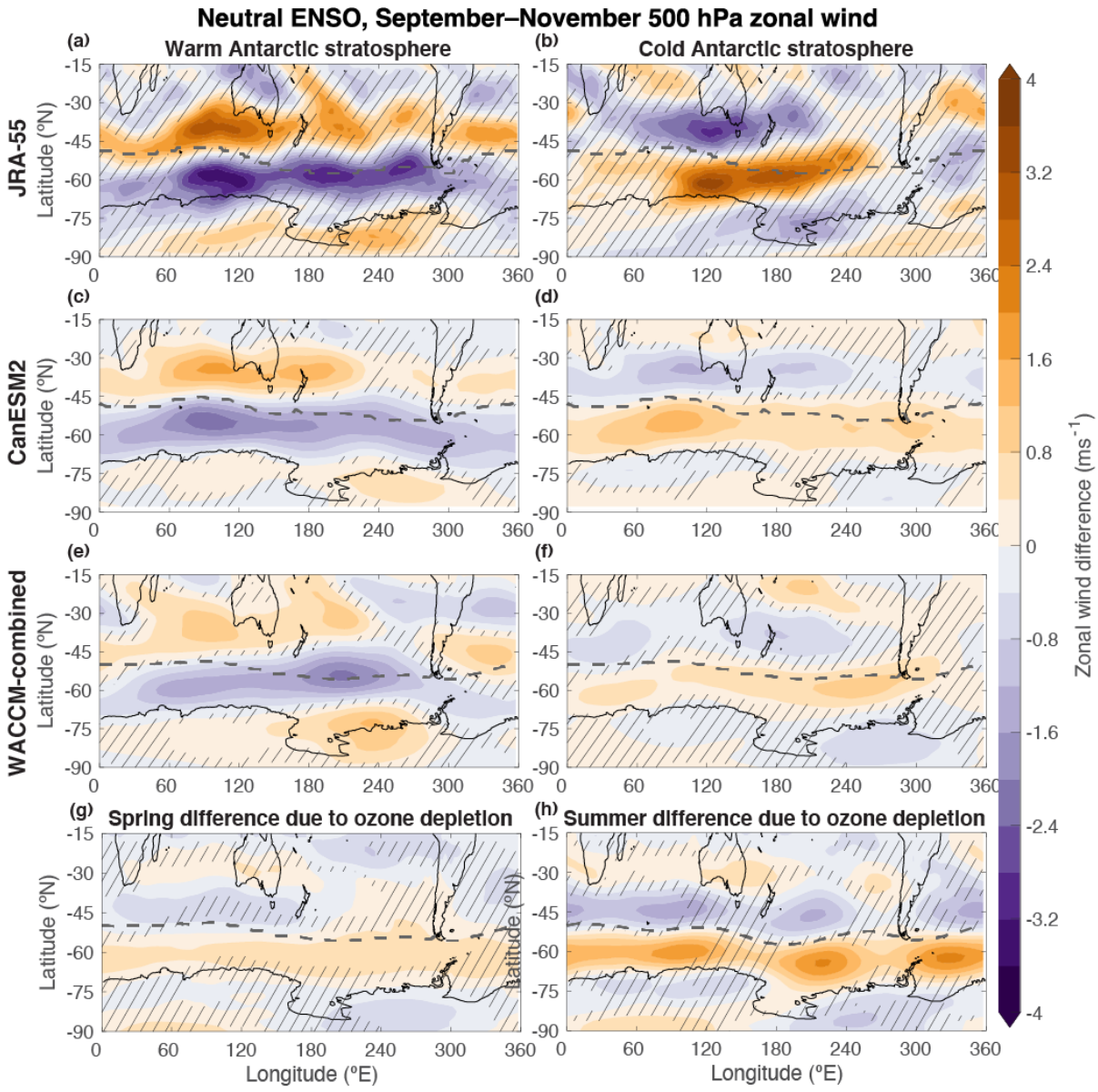

951

952 **Figure 8.** September–November 500 hPa zonal wind response to Antarctic stratospheric
953 extremes that occur during a neutral June–August ENSO for JRA-55 (a and b), CanESM2 (c
954 and d), and WACCM-combined (e and f). Panels g and h show the ozone hole depletion
955 influence through the difference between the WACCM-GHG_HODS_H and WACCM-
956 GHG_HODS_L ensembles for spring and summer respectively. Dashed lines indicate the
957 latitudes of climatological maximum zonal wind. Hatching shows where differences are not
958 significantly different from each other ($p < .1$) using a two-tailed t-test.

959

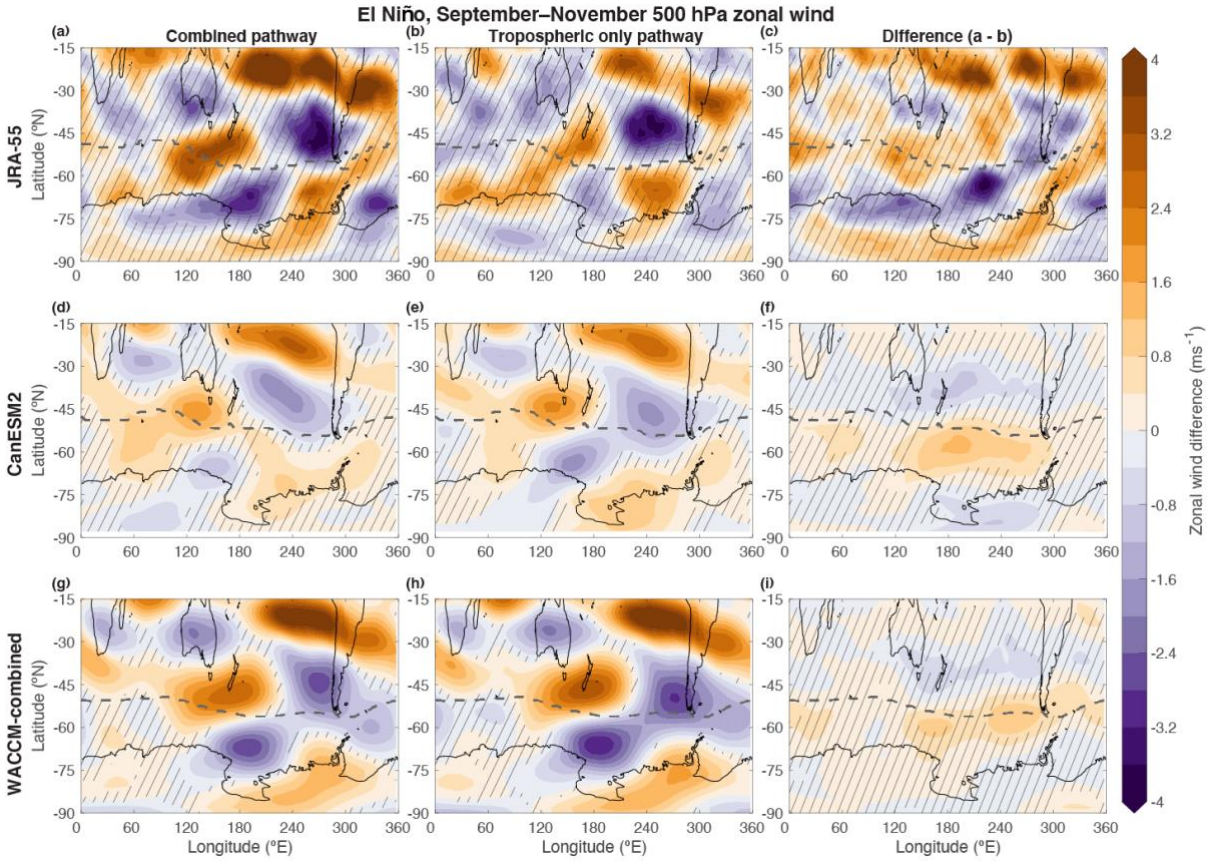

960

961 **Figure 9.** 500 hPa zonal wind El Niño composite anomalies for subsets: combined and
962 tropospheric only pathways (See Figure 7) during September–November for JRA-55,
963 CanESM2, and WACCM-combined. Dashed lines indicate the latitudes of climatological
964 maximum zonal wind. Hatching shows where differences are not significantly different from
965 each other ($p < .1$) using a two-tailed t-test.

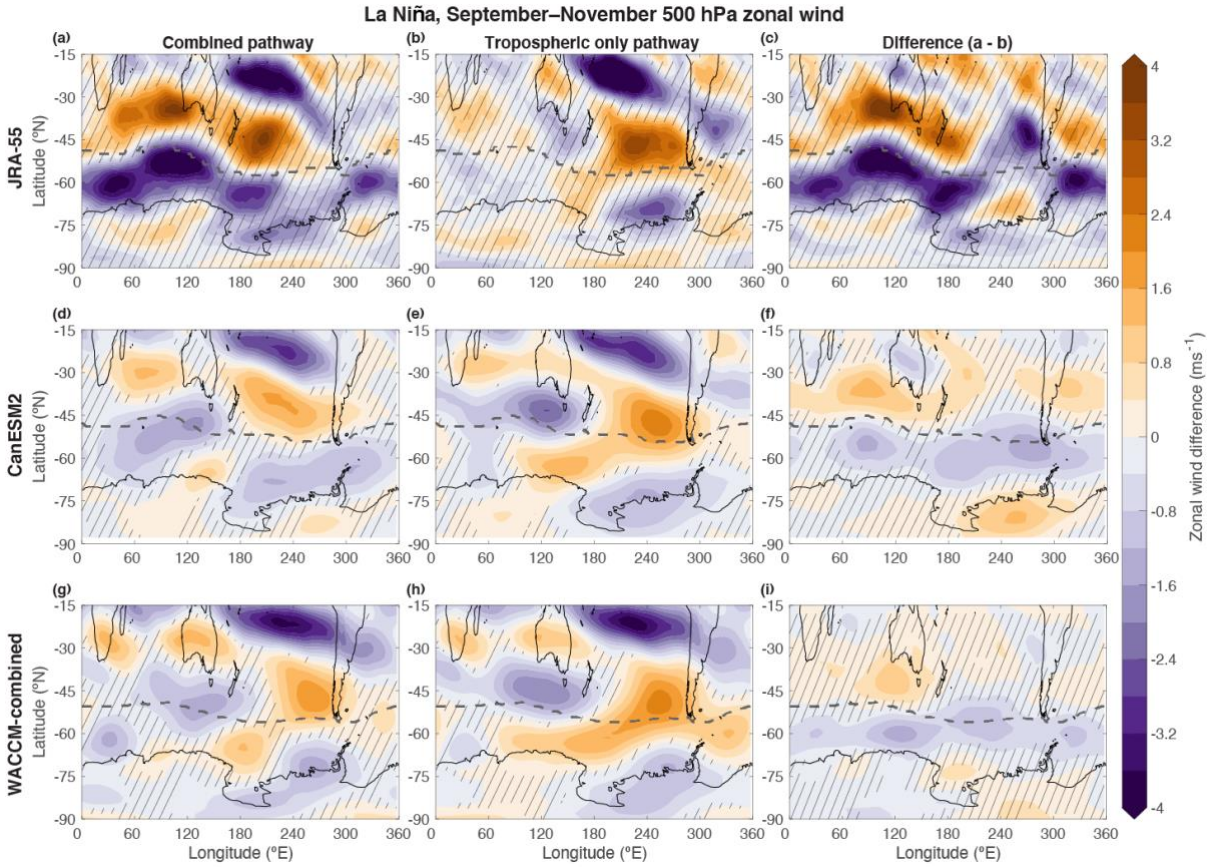

966

967 **Figure 10.** Same as Figure 9, but for September–November La Niña composite anomalies.

968

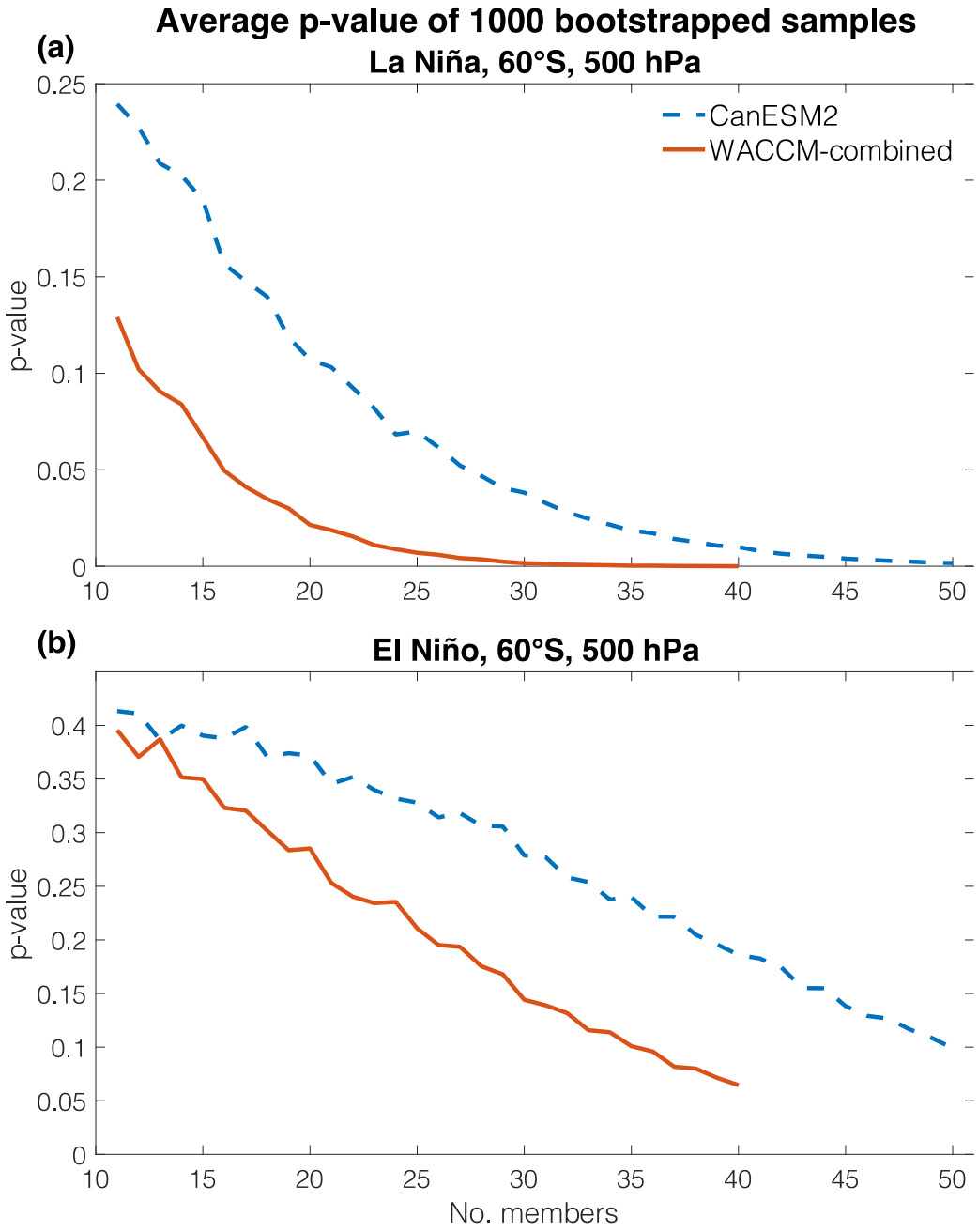

969

970 **Figure 11.** Average p-values for the number of ensemble members used to calculate the
971 difference between the combined and tropospheric only pathways after a 1000 bootstrap
972 process of random members within the 40-member pool for WACCM-combined and 50-
973 member pool for CanESM2. P-values were calculated from a two-sided t-test between the
974 two datastes, corresponding to figures 9 and 10, panels f and i.

975

Supporting information for: On the Southern Hemisphere stratospheric response to ENSO and its impacts on tropospheric circulation

Kane A. Stone[a], Susan Solomon[a], David W. J. Thompson[b], Douglas E. Kinnison[c], John C. Fyfe[d]

Table S1. JRA-55 SH stratospheric ENSO response years

El Niño response years (cold stratosphere)	El Niño years without stratospheric response	La Niña response years (warm stratosphere)	La Niña years without stratospheric response
1987	1972	1964	1971
1997	1982	1970	1973
2015	1993	1988	1974
	2009	2007	1975
		2013	1999
			2010
			2011

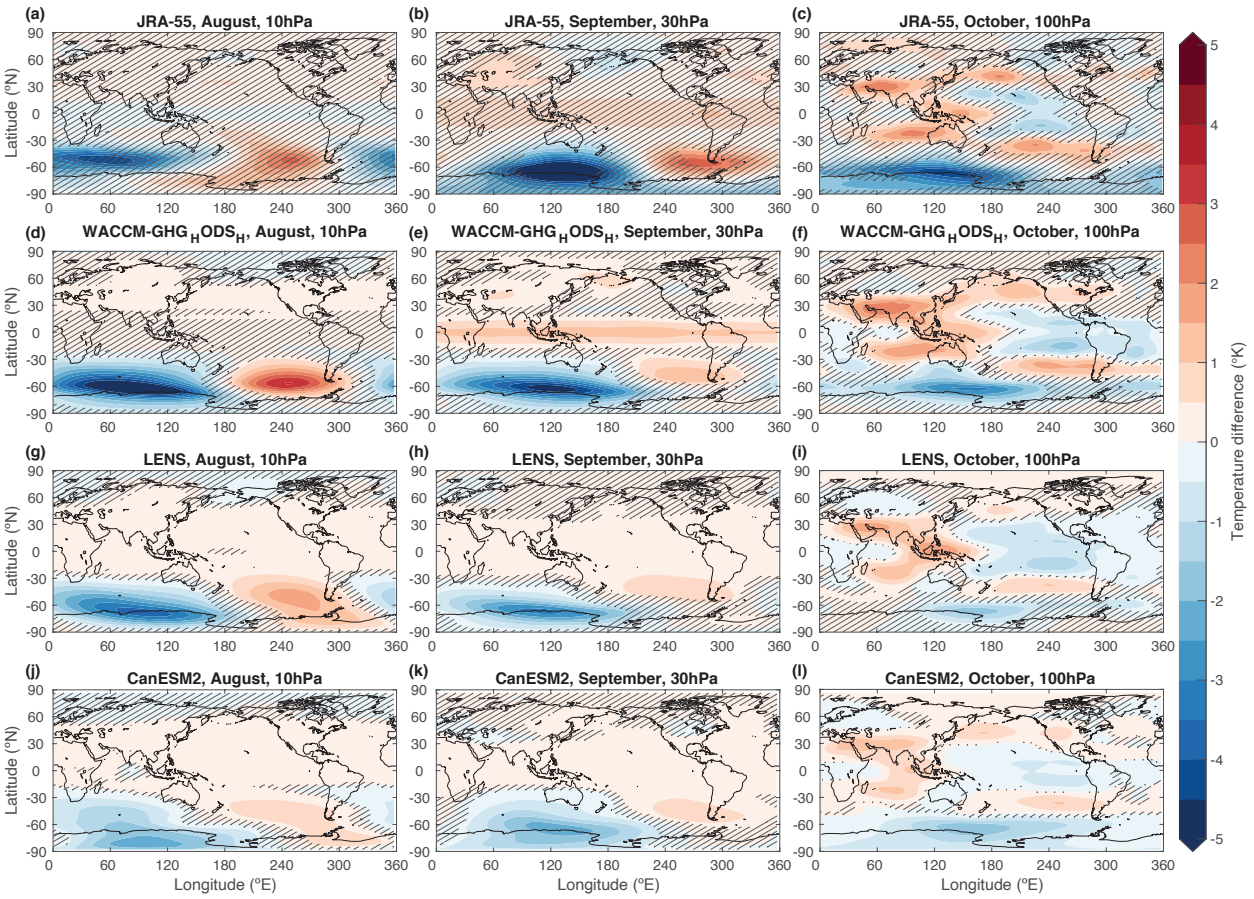

Figure S1. June–August El Niño composite anomalies of August 10 hPa, September 30 hPa, and October 100 hPa temperatures for JRA-55 (a, b, c), WACCM-GHG$_H$ODS$_H$ (d, e, f), LENS (g, h, i), and CanESM2 (j, k, l). Hatching shows areas that are not significant to the 90th percentile following a two-sided student t-test.

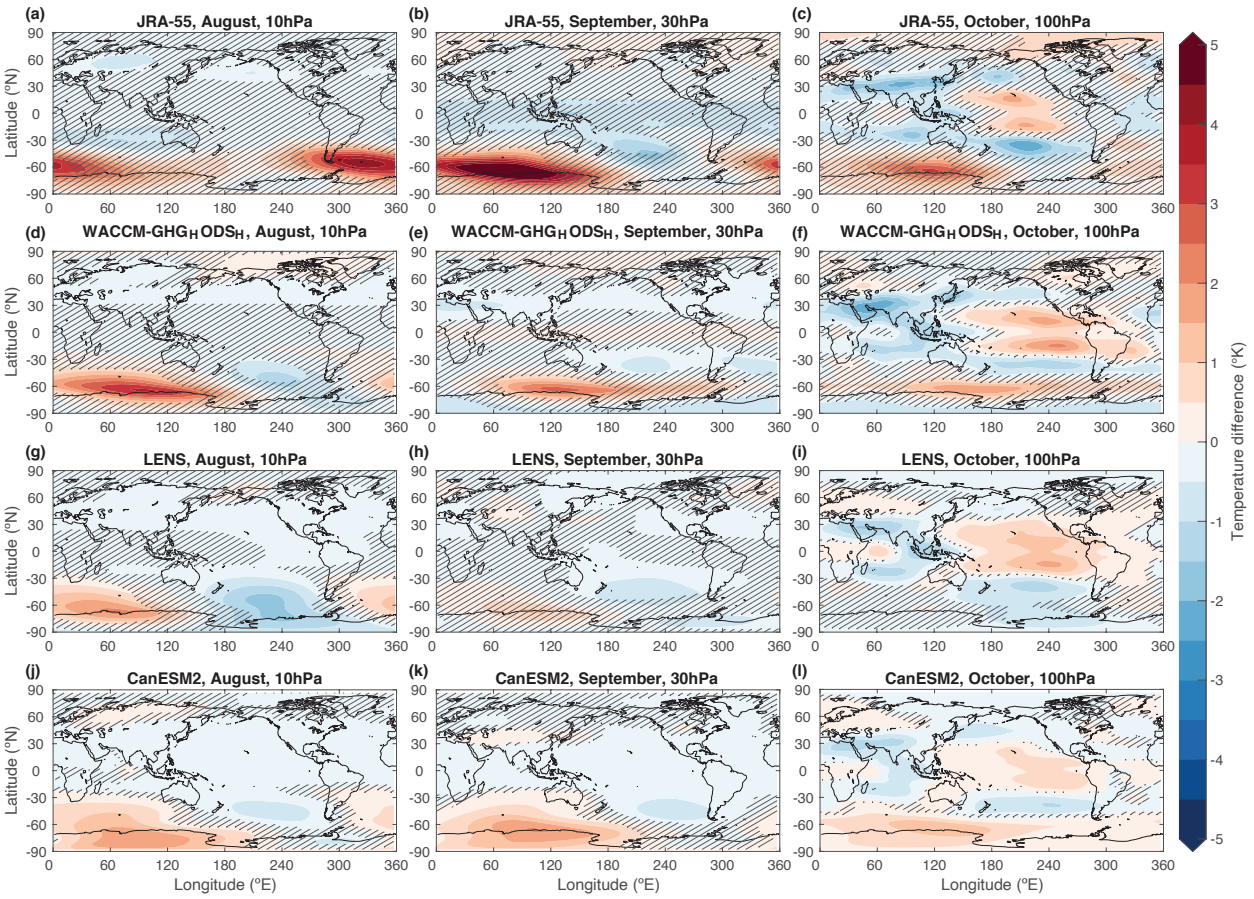

Figure S2. Same as figure S2, but for June–August La Niña composite anomalies.

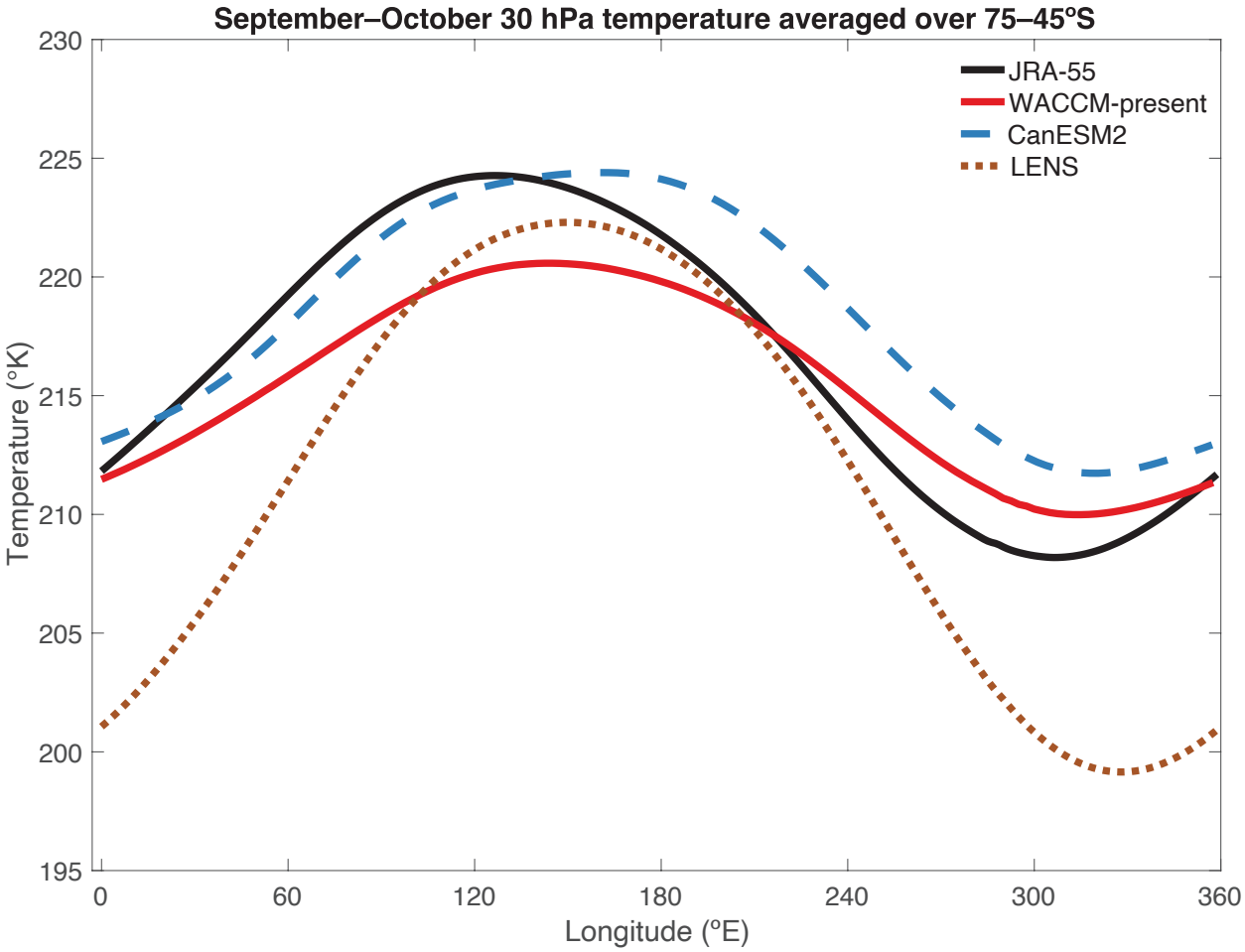

Figure S3. Temperatures averaged over 75–45˚S for JRA-55, WACCM-present, CanESM2, and LENS for September–October at 30hPa highlighting the large LENS wave-1 amplitude.

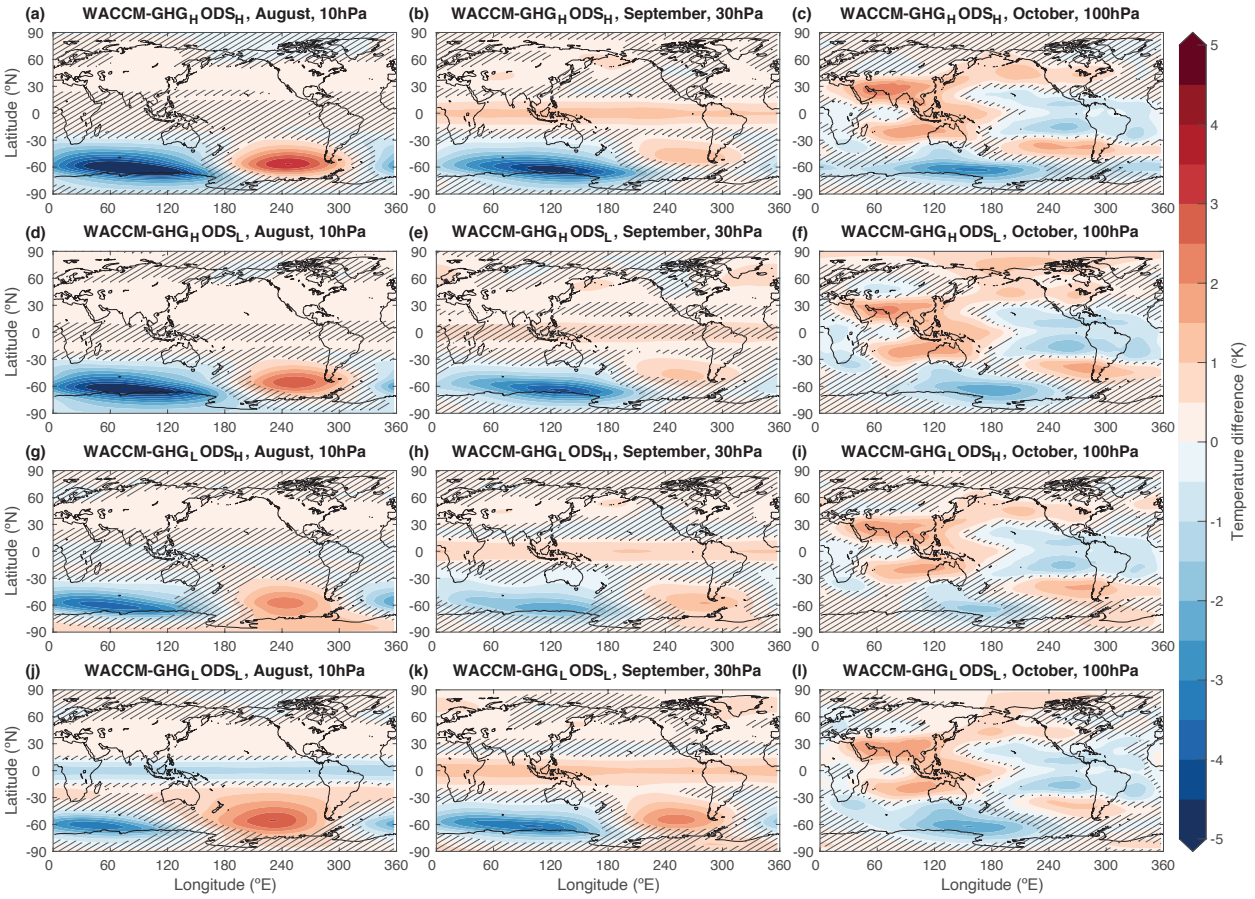

Figure S4. June–August El Niño composite anomalies of August 10 hPa, September 30 hPa, and October 100 hPa temperatures for WACCM-GHG$_H$ODS$_H$ (a, b, c), WACCM-GHG$_H$ODS$_L$ (d, e, f), WACCM-GHG$_L$ODS$_H$ (g, h, i), and WACCM-GHG$_L$ODS$_L$ (j, k, l). Hatching shows areas that are not significant to the 95th percentile following a two-sided student t-test.

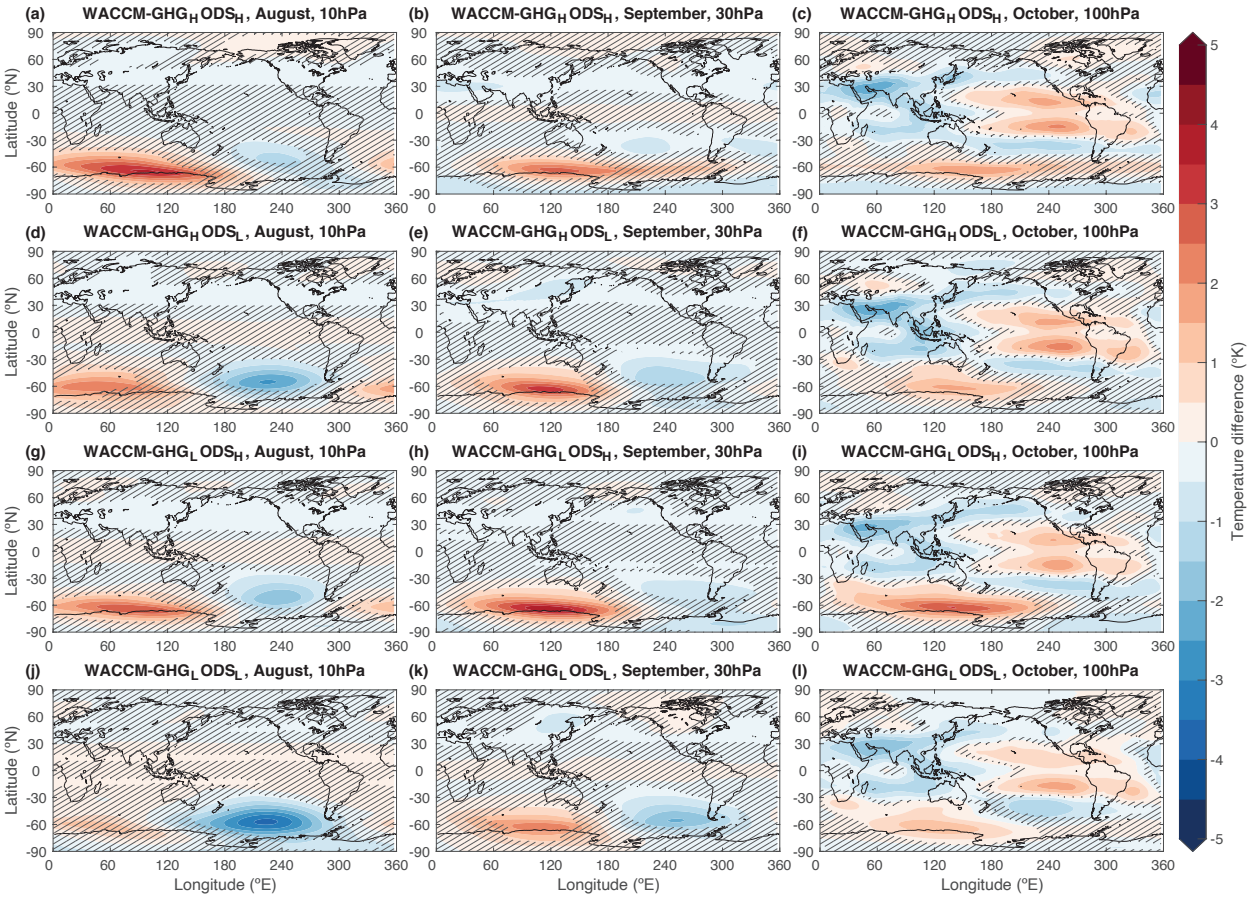

Figure S5. Same as Figure S4, but for June–August La Nina composite anomalies.

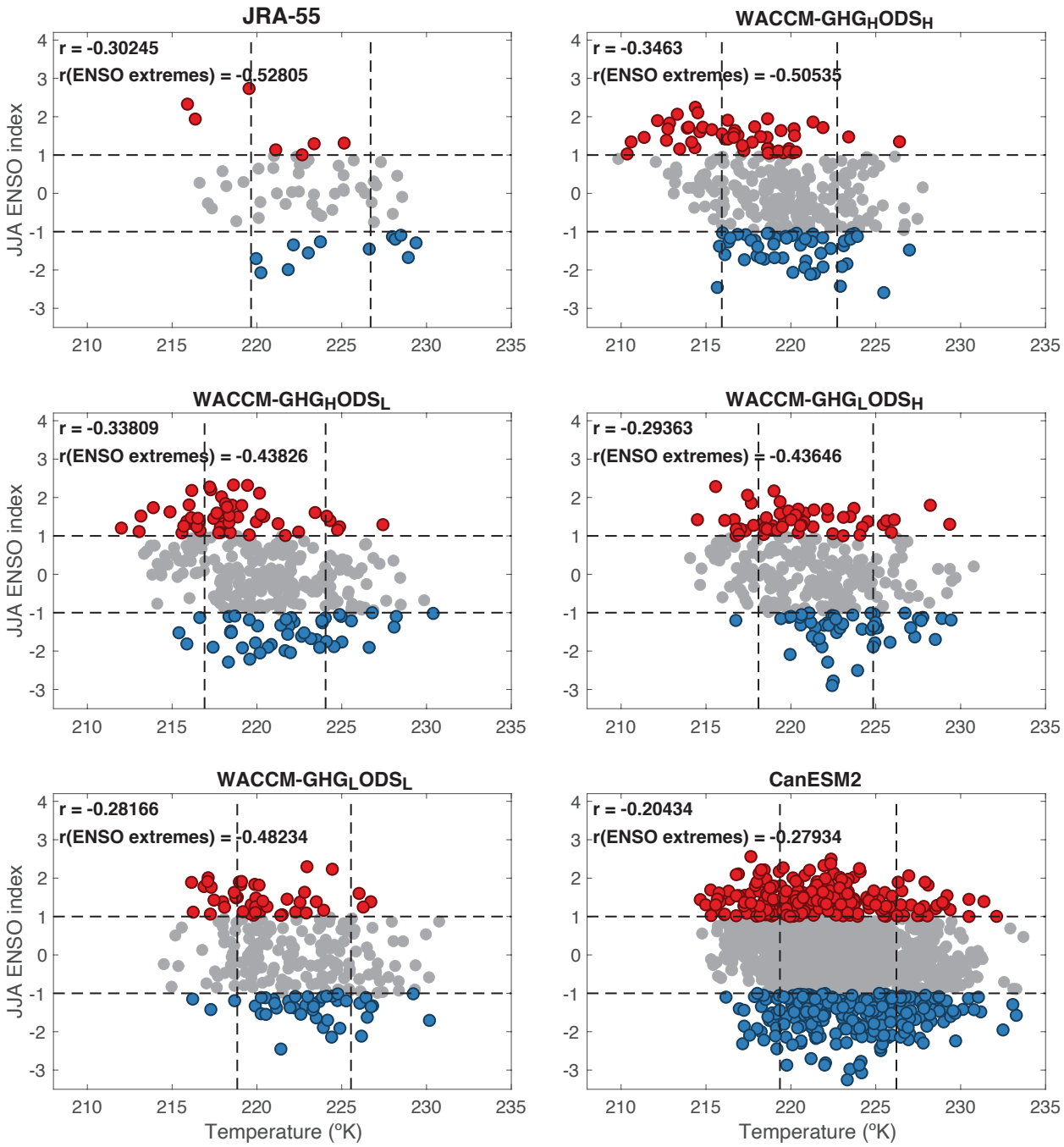

Figure S6. Scatter plot of September–October 30 hPa temperatures averaged over 75–45˚S and 60–180˚E and June–August ENSO event for JRA-55, the WACCM ensembles and CanESM2. Correlations are shown for all data and for data that corresponds to an ENSO extreme (greater or less than 1). R values are Pearson correlation coefficients between ENSO and temperature. For r(ENSO extremes), only ENSO years above or below 1 and -1 standard deviations where used to calculate the correlations. All correlations are significantly different than zero ($p < .05$).

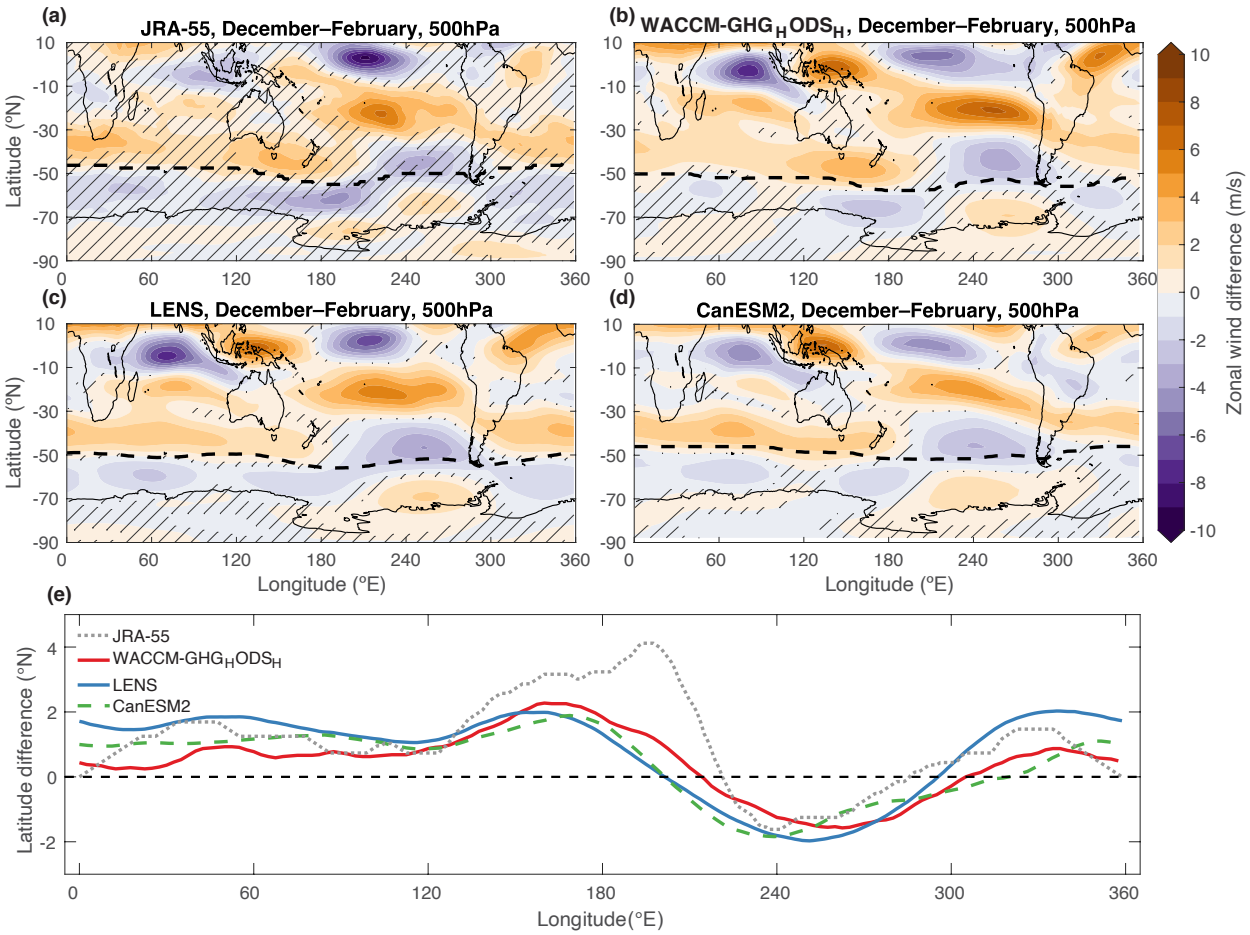

Figure S7. Same as Figure 5, but for December–February.

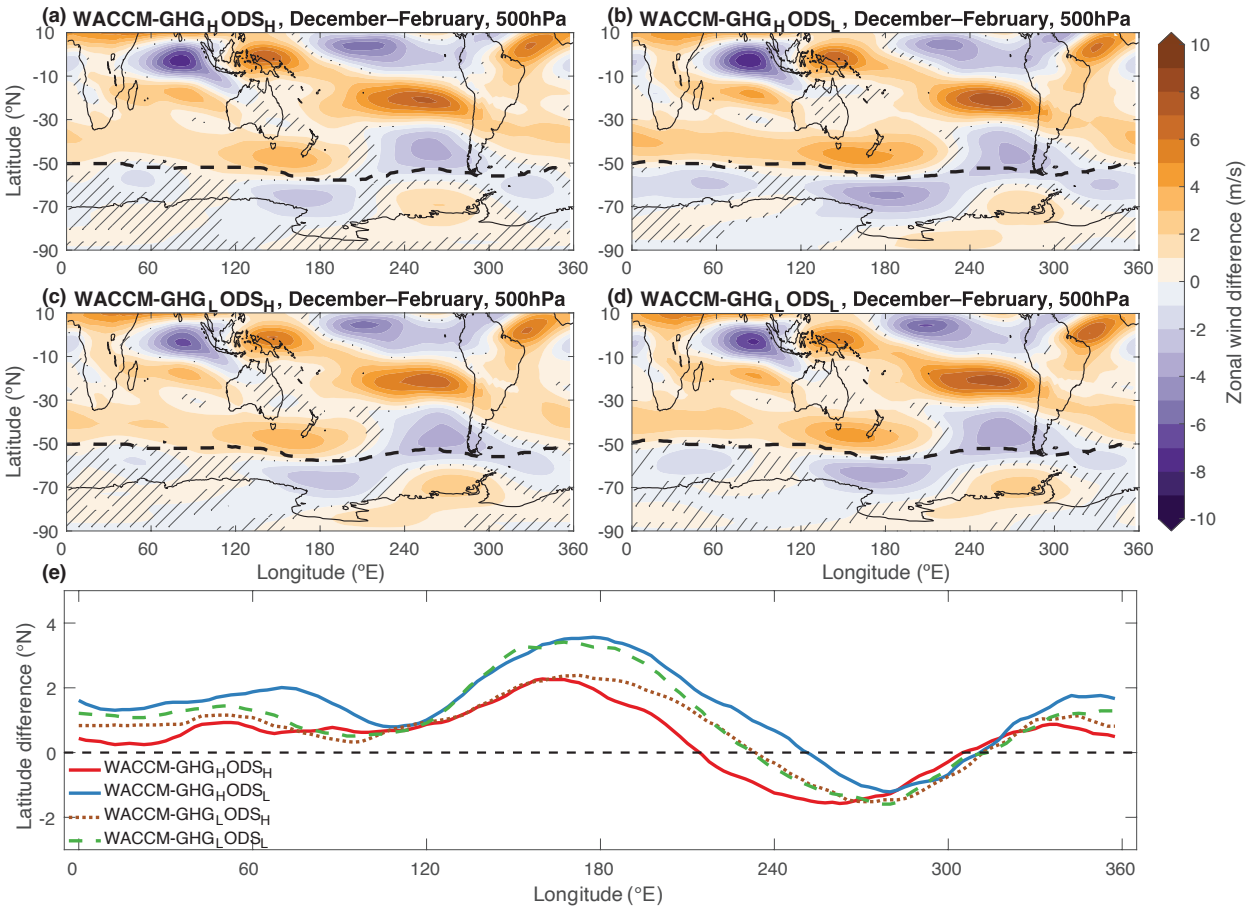

Figure S8. Same as Figure 6, but for December–February.

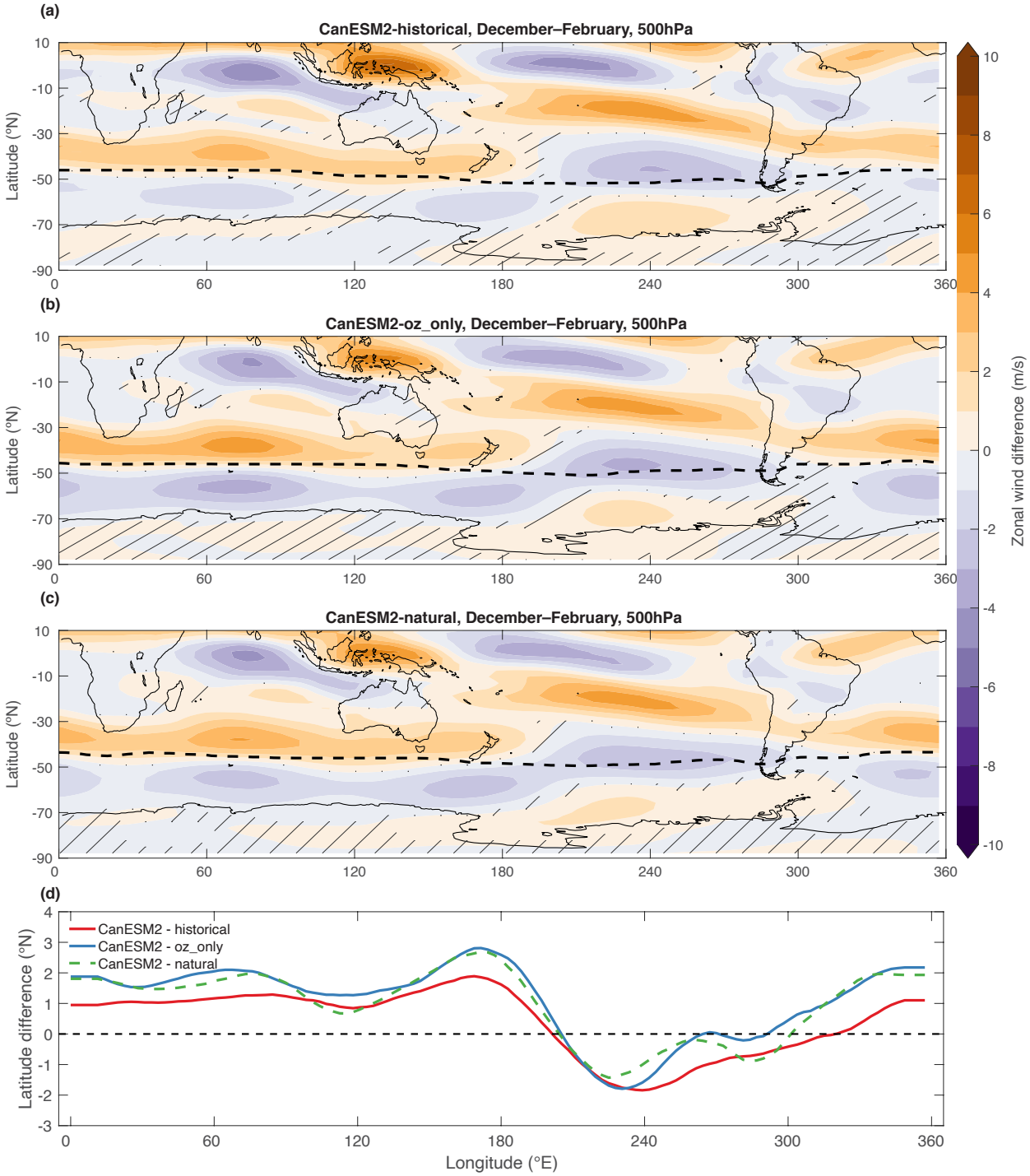

Figure S9. Same as Figure S8, except for CanESM2-historical, CanESM2-oz_only, and CanESM2-natural. CanESM2-oz_only has only prescribed ozone forcings, and CanESM2-natural has pre-industrial forcings. All three ensembles consist of 50 members. CanESM2-historical and CanESM2-oz_only have a period from 1995–2025, while CanESM2-natural has a period of 1990–2020. CanESM2-historical is the same ensemble as used in the main paper. Stippling indicates significance at the 95th percentile following a student t-test.

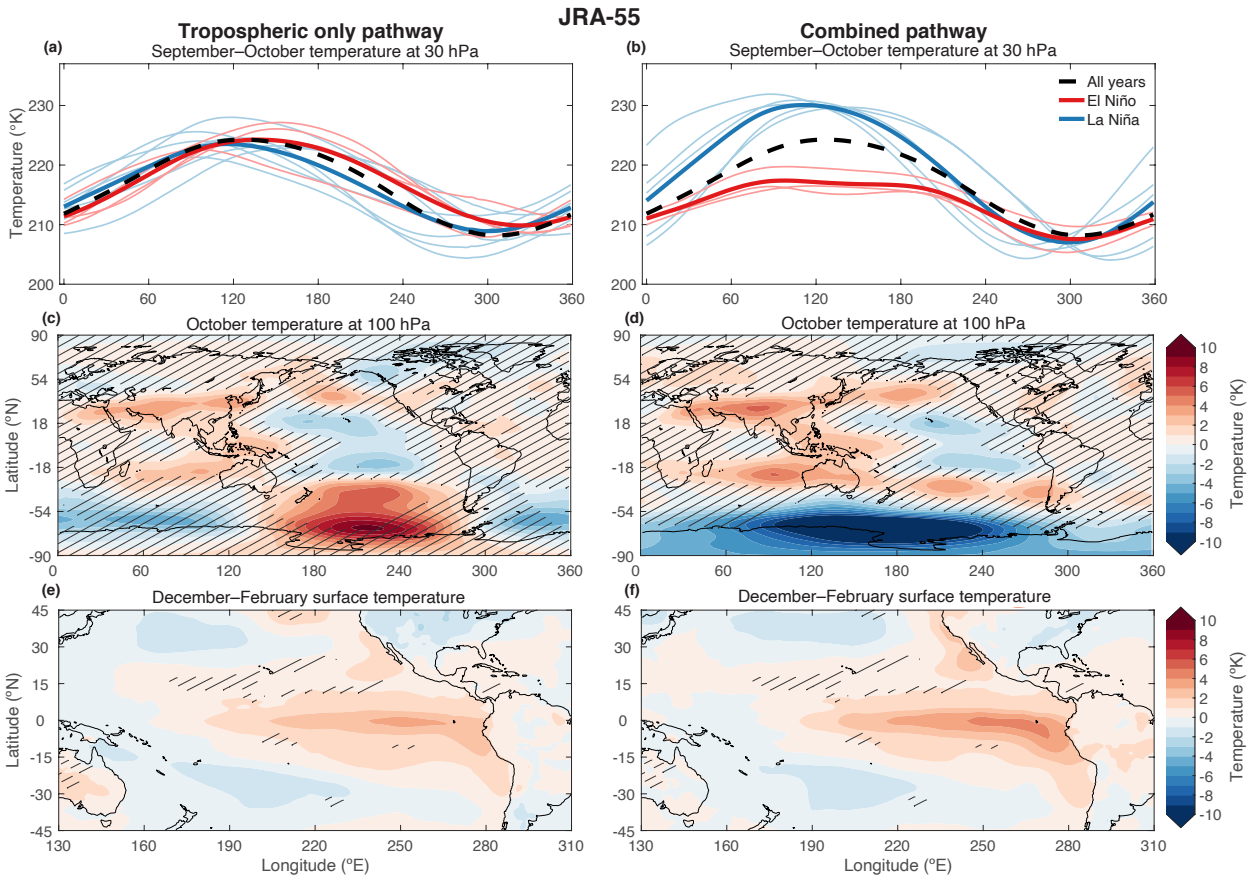

Figure S10. Same as Figure 7, but for JRA-55

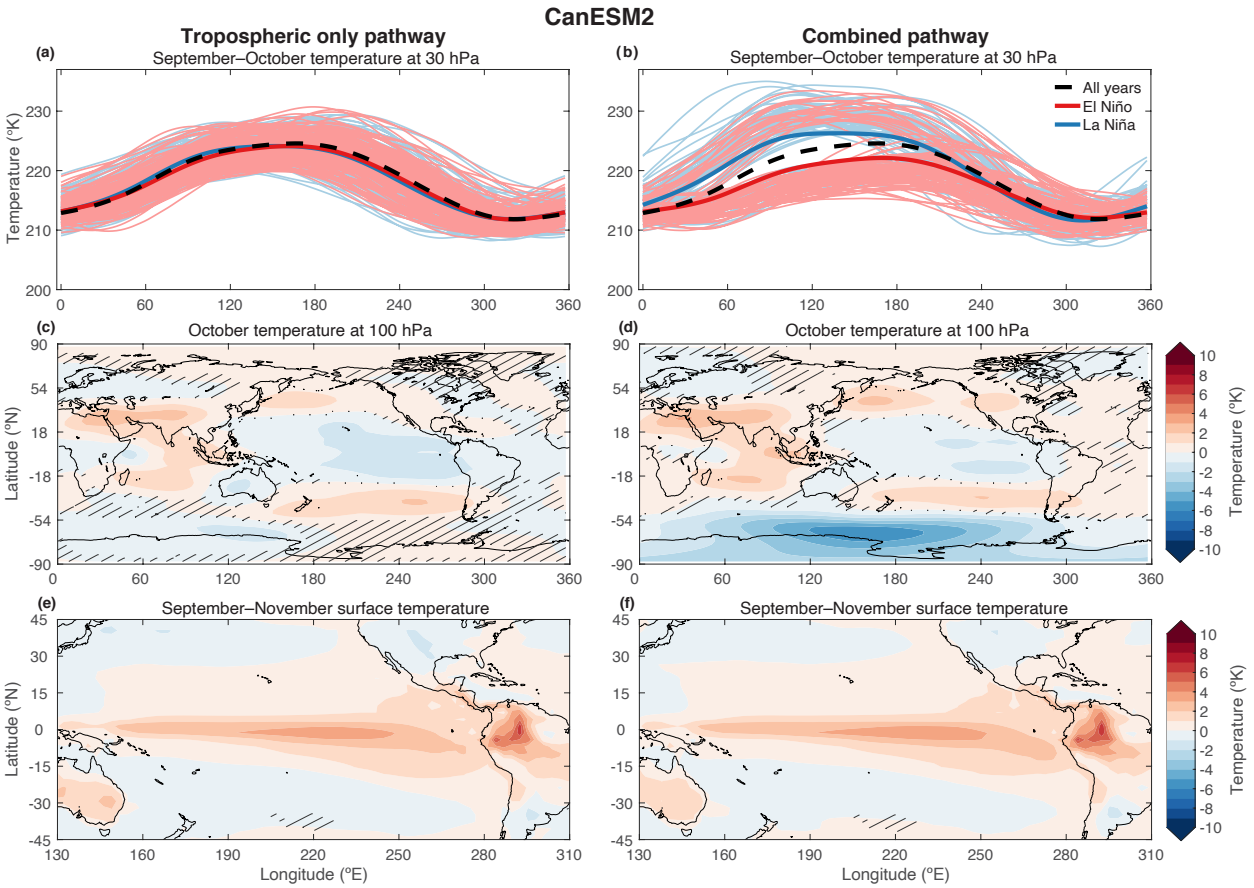

Figure S11. Same as Figure 7, but for CanESM2.

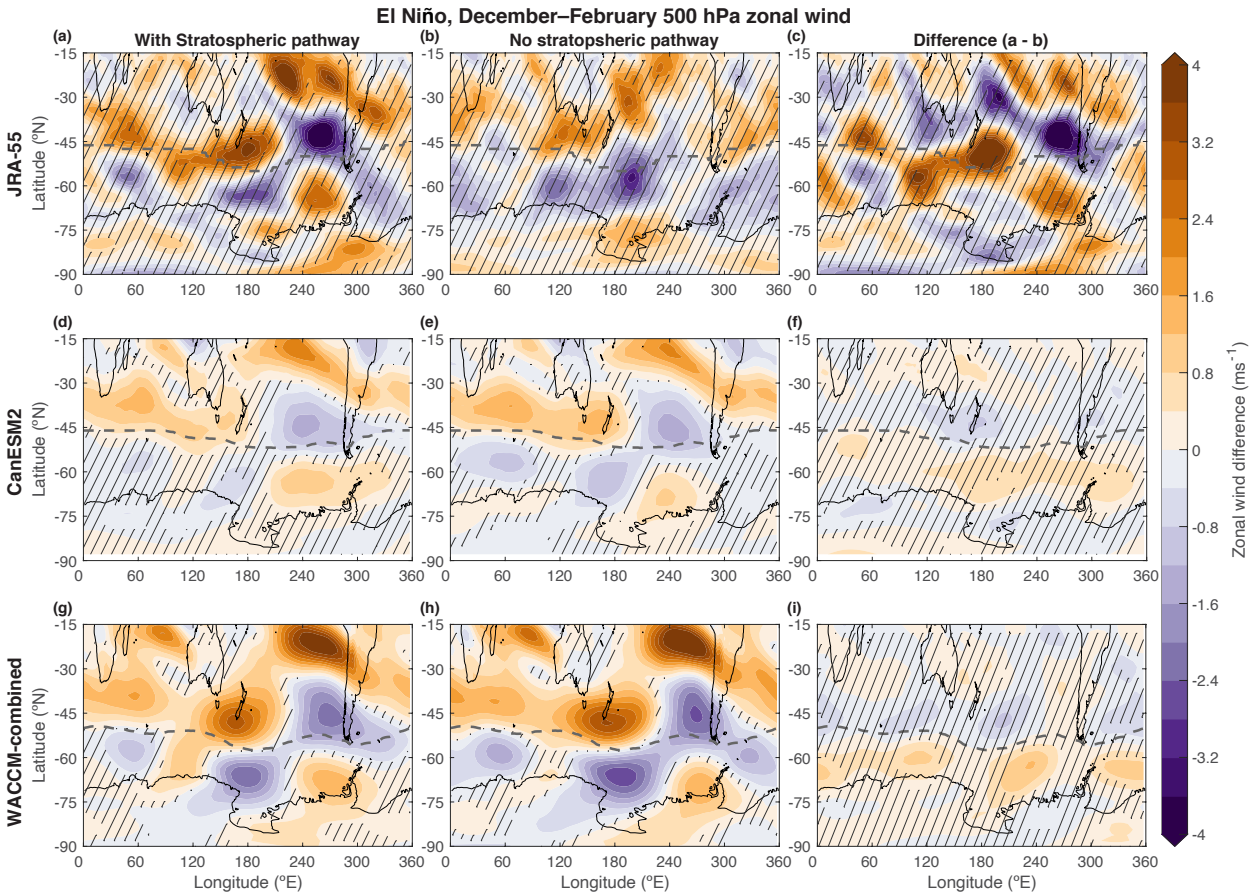

Figure S12. Same as Figure 9, but for December–February.

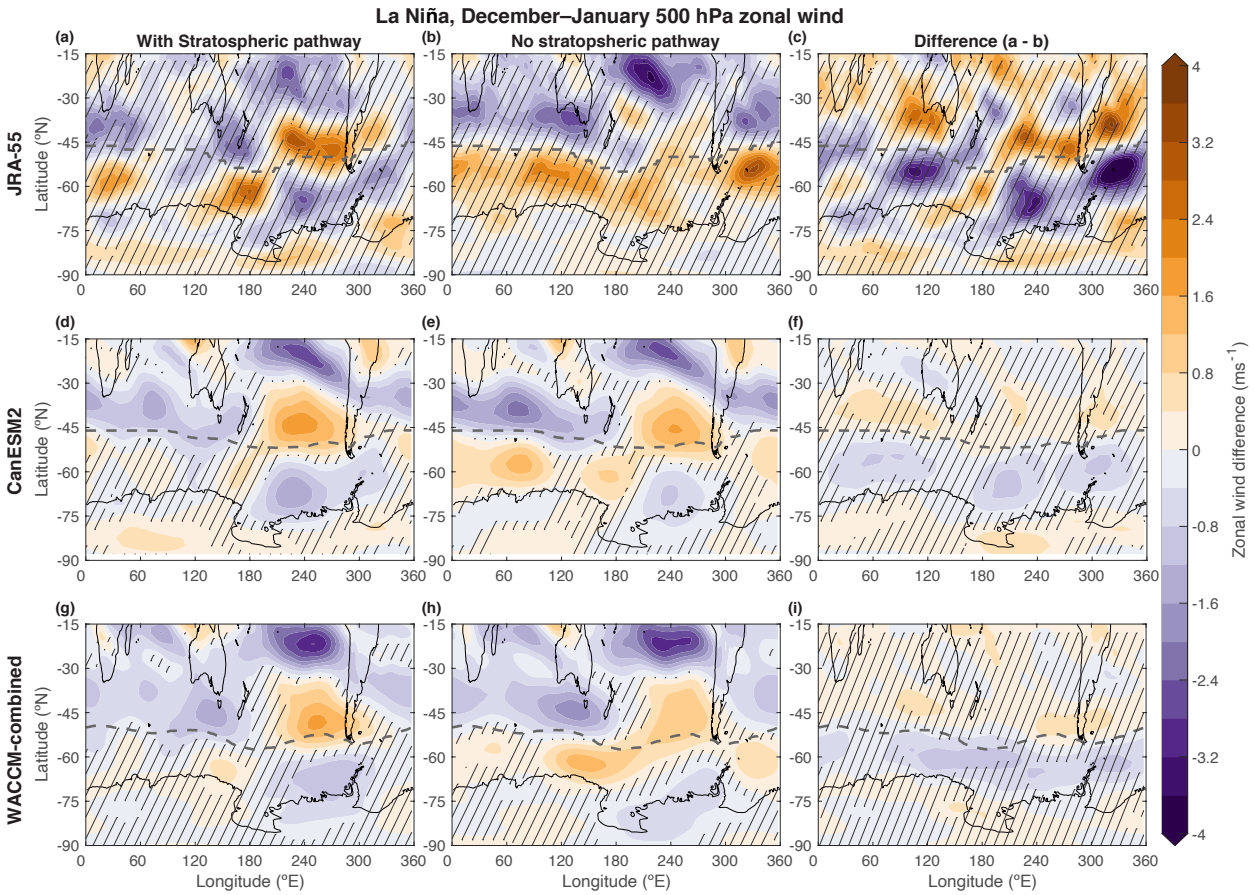

Figure S13. Same as Figure 10, but for December–February.